The Astrophysical Journal, 833:55 (19pp), 2016 December 10 doi:10.3847/1538-4357/833/1/55

TRACING INFALL AND ROTATION ALONG THE OUTFLOW CAVITY WALLS OF THE L483 PROTOSTELLAR ENVELOPE

Gigi Y. C. Leung[1], Jeremy Lim[1,2], and Shigehisa Takakuwa[3]
[1] Department of Physics, University of Hong Kong, Pok Fu Lam Road, Hong Kong
[2] Laboratory for Space Research, Faculty of Science, The University of Hong Kong, Pokfulam Road, Hong Kong
[3] Academia Sinica Institute of Astronomy and Astrophysics, P.O. Box 23-141, Taipei 10617, Taiwan
Received 2015 August 1; revised 2016 October 2; accepted 2016 October 6; published 2016 December 7

ABSTRACT

Single-dish observations in CS(7–6) reveal emission extending out to thousands of au along the outflow axis of low-mass protostars and having a velocity gradient in the opposite direction to that of their outflows. This emission has been attributed to dense and warm gas flowing outward along the walls of bipolar outflow cavities. Here, we present combined single-dish and interferometric CS(7–6) maps for the low-mass protostar L483, revealing a newly discovered compact central component (radius $\lesssim$800 au) and previously unknown features in its extended component (visible out to ~4000 au). The velocity gradient and skewed (toward the redshifted side) brightness distribution of the extended component are detectable out to a radius of ~2000 au, but not beyond. The compact central component exhibits a velocity gradient in the same direction as, but which is steeper than that of, the extended component. Furthermore, both components exhibit a velocity gradient with an approximately constant magnitude across the outflow axis, apparent in the extended component not just through but also away from the center out to 2000 au. We point out contradictions between our results and model predictions for outflowing gas and propose a new model in which all of the aforementioned emission can be qualitatively explained by gas inflowing along the outflow cavity walls of a rigidly rotating envelope. Our model also can explain the extended CS(7–6) emission observed around other low-mass protostars.

Key words: stars: protostars

1. INTRODUCTION

Stars are born in dense condensations, referred to as cores, in molecular clouds. A comparison between the prestellar core mass function and the initial mass function indicates that only about one-third of the core mass is accreted by the embedded star or stellar system (e.g., review by Offner et al. 2014, p. 53). Given the comparatively low masses contained in circumstellar disks around young stellar objects, the bulk in mass of their natal cores must be dispersed. The underlying processes that drive this dispersal remain poorly understood, although the most visible manifestation is a bipolar outflow (e.g., review by Frank et al. 2014, p. 451).

One of the most widely cited mechanisms for dispersing protostellar envelopes is entrainment by a bipolar outflow driven (through magnetohydrodynamics processes) from a circumstellar disk. Highly collimated jets with velocities of typically $\gtrsim$100 km s^{-1}, readily detectable at radio to optical wavelengths, are widely attributed to such a (primary) bipolar outflow. By contrast, the entrained material usually comprises a pair of poorly collimated lobes with velocities of typically only ~10 km s^{-1}, most commonly detected in the rotational transitions of carbon monoxide (CO) at millimeter and submillimeter wavelengths and hence referred to as bipolar molecular outflows. To produce the wide opening angles of bipolar molecular outflows, a wide-angle wind is invoked, in addition to the jet, to sweep up the protostellar envelope. Indeed, such wide-angle winds are predicted in models where the wind is driven from the circumstellar disk of a protostar, specifically in both the X-wind (Shu et al. 1997) and disk wind (Ferreira 1997; Pudritz et al. 2007, p. 277) models.

Observations of bipolar molecular outflows at high angular resolution with radio interferometers have shown an increasing opening angle at their base from Class 0 to Class I sources (i.e., low-mass protostars; Arce & Sargent 2006). A similar trend has also been found for their outflow cavities as traced in scattered light through infrared observations (Seale & Looney 2008). These results have been reproduced in simulations where the angular distribution of injected momentum remains constant over time in a wind that has a density decreasing away from the outflow axis, corresponding to the rotation axis of the circumstellar disk (Offner et al. 2011). Such an intrinsically wide-angle wind can appear as a jet in observations where the emitted light intensity is proportional to the square of the gas density, as is the case for free–free continuum emission at radio to optical wavelengths or atomic/ionic line emission at infrared and optical wavelengths. Early in the evolution of a protostar, only the densest axial component of the wind is able to puncture through the protostellar envelope, thus producing a bipolar molecular outflow or a corresponding outflow cavity having a relatively narrow opening angle. Over time, material in the protostellar envelope at larger angles to the wind axis as subtended from the protostar is progressively swept away, resulting in a bipolar molecular outflow or corresponding outflow cavity with an ever-widening opening angle at the base. On the other hand, studies by Hatchell et al. (2007) and Curtis et al. (2010) have found that the mass-flux rates in the bipolar molecular outflows of both Class 0 and Class I sources are too low (by about an order of magnitude) to disperse their envelopes within a disappearance timescale of order 10^5 yr. If so, then the observed broadening at the base of bipolar molecular outflows or bipolar outflow cavities with age is not a cause, but rather a consequence, of envelope dispersal. Measurements of the mass-flux rates in bipolar molecular outflows, however, are complicated by uncertainties in line opacities, excitation, and gas at low velocities confused with the ambient envelope.

From single-dish observations of both Class 0 and I sources with the Atacama Submillimeter Telescope Experiment (ASTE), Takakuwa et al. (2007) and Takakuwa & Kamazaki (2011) found that their CS(7–6) and HCN(4–3) emissions are elongated along the outflow axis and have an opposite direction in velocity gradient to their corresponding bipolar CO outflows. They attributed the observed emissions to relatively dense and warm molecular gas lifted from the walls of the outflow cavities and dispersed outward. This explanation requires a particular geometry such that the cavity walls producing the observed extended CS(7–6) and HCN(4–3) emission are located on the opposite side of the sky plane relative to the outflow axis, thus giving rise to an opposite direction in velocity gradient between gas dispersed along the cavity walls and that dispersed closer to the outflow axis (i.e., the bipolar CO outflow). If correctly interpreted, the highly extended CS (7–6) and HCN(4–3) emission therefore traces the active dispersal of protostellar envelopes through the evacuation of bipolar outflow cavities. Measurements of the mass-flux rate in the outflowing gas would enhance our understanding of the degree to which protostellar envelopes are dispersed through a bipolar outflow.

The model proposed by Takakuwa & Kamazaki (2011) makes a number of specific predictions that can be readily tested. First, the direction in velocity gradient exhibited by the hypothesized outflowing gas depends on the outflow cavity geometry, and under the appropriate circumstances it can be the same as the bipolar CO outflow. Second, unless the outflow axis is close to the sky plane, the model predicts a relatively compact central component corresponding to the cavity walls closer to the line of sight. In this manuscript, we combine single-dish and interferometric data for the protostar L483, previously published separately, to study the spatial-kinematic structure of its CS(7–6) emission over a wide range of spatial scales. Located at a distance of ∼200 pc, L483 is believed to be transitioning from Class 0 to Class I. It exhibits features typical of Class 0 protostars, such as a low bolometric temperature of 50 K and a redward asymmetry in single-dish spectra indicative of motion dominated by infall, but on the other hand an outflow that is less chemically abundant than typical Class 0 protostars (Tafalla et al. 2000).

L483 was one of the seven objects mapped by Takakuwa et al. (2007) and Takakuwa & Kamazaki (2011) with the ASTE in both CS(7–6) and HCN(4–3). This object also has been mapped in CS(7–6), as well as in a number of other molecular lines, with the Submillimeter Array (SMA) by Jørgensen et al. (2007). By contrast with the extended CS(7–6) emission seen in the ASTE map, their SMA map shows only weak and unresolved CS(7–6) emission coincident with the protostar. To date, combined single-dish and interferometric maps in CS (7–6) have been reported only for B335 (Yen et al. 2011) and L1551 IRS 5 (Takakuwa & Kamazaki 2011). By contrast with L483, B335 has an outflow axis close to the plane of the sky, nullifying one of the important predictions of the model proposed by Takakuwa & Kamazaki (2011). In the case of L1551 IRS 5, the likely presence of a centrally condensed circumbinary envelope and/or a circumbinary disk complicates the interpretation of its relatively compact CS(7–6) emission. As we shall show, the spatial-kinematic structure of the CS (7–6) emission from L483 is much more complex than is revealed in either the previously published single-dish or interferometric map alone. Furthermore, a full explanation for all of the features that we find requires an entirely different model than that proposed by Takakuwa & Kamazaki (2011).

Readers interested in the data used, which include the ^{12}CO (2–1) and ^{13}CO(2–1) lines, and the manner in which the single-dish and interferometric data in CS(7–6) were combined should proceed to Section 2. Readers interested only in the results can skip ahead to Section 3. In Section 4, we demonstrate that, apart from emission associated with a bipolar CO outflow, the remaining emissions in both ^{12}CO(2–1) and ^{13}CO(2–1) and all that in CS(7–6) trace inflowing, rather than outflowing, gas along the cavity walls of a rotating envelope. In Section 5, we show that our model also can be successfully applied to explain the CS(7–6) emission observed from L1551 IRS 5 and provides a superior explanation for the CS(7–6) emission observed from B335. A thorough summary of our results and interpretation can be found in Section 6.

2. DATA REDUCTION

2.1. SMA

We retrieved the original data on L483 previously published by Jørgensen et al. (2007) from the SMA archive. These data formed part of the Submillimeter Array Survey of Low-Mass Protostars (SMA) PROSAC program. The observations of L483 were carried out at 0.8 mm (342 GHz) on 2005 July 10 and 1.3 mm (230 GHz) on 2005 July 24. In the observation at 1.3 mm, the ^{12}CO(2–1), ^{13}CO(2–1), and C^{18}O(2–1) lines were detected. In the observation at 0.8 mm, only the CS(7–6) line was detected. The channel width employed in the observations was 1.1 km s^{-1} for ^{12}CO(2–1), 0.28 km s^{-1} for ^{13}CO(2–1) as well as C^{18}O(2–1), and 0.18 km s^{-1} for CS(7–6). During both observations, the SMA was in its compact configuration, providing shortest projected baselines of 10 kλ at 1.3 mm and 12 kλ at 0.8 mm. Owing to the lack of even shorter baselines, emission smoothly distributed on angular scales $\gtrsim$20″ at 1.3 mm and $\gtrsim$17″ at 0.8 mm would have been largely resolved out; furthermore, only a fraction of the emission approaching these angular scales would have been recovered.

We reduced the data using the MIR-IDL package. In both observations, the same sets of calibrators were observed for the purpose of primary, secondary, and bandpass calibration. We used the planet Uranus and Jupiter's moon Callisto, along with the two quasars 3C 454.3 and 3C 279, for bandpass calibration. At short baselines, Uranus and Callisto provide a higher signal-to-noise ratio (S/N) than the two quasars. At long baselines, however, both Uranus and Callisto are strongly resolved; on such baselines, the quasars provide a better S/N. All these calibrators were therefore used to generate an optimal bandpass solution for each antenna. To derive complex gains corrections (i.e., corrections for variations in amplitude and phase caused by the Earth's atmosphere or telescope electronics), we used the quasar 1743-038, which is located ∼10° from L483. Antenna-based complex gain corrections were derived for all the antennas but one, which showed significant baseline-based errors. For this antenna, we therefore derived baseline-based complex gain corrections. Uranus was used for absolute flux calibration.

After calibration, we transferred the data to the software package MIRIAD (Sault et al. 1995) for further processing. We generated a continuum map at each of the wavelength bands observed from the line-free channels. In all, a total bandwidth of 4 GHz at both 1.3 mm and 0.8 mm was available for

Table 1
Map Parameters

Maps	Telescope	Weighting	FWHM of Gaussian Taper	Synthesized Beam (Jy beam^{-1})	rms Noise	Figures
1.3 mm continuum	SMA	Natural	…	$3\farcs80 \times 3\farcs17$, P.A. = 26.9°	0.003	1(a)
0.8 mm continuum	SMA	Natural	…	$2\farcs41 \times 2\farcs30$, P.A. = 47.4°	0.004	1(b)
^{12}CO(2–1)	SMA	Natural	…	$3\farcs72 \times 3\farcs10$, P.A. = 26.9°	0.21	2, 5(a), 5(c)
^{13}CO(2–1)	SMA	Natural	…	$3\farcs89 \times 3\farcs24$, P.A. = 26.9°	0.3	3, 5(b), 5(d)
CS(7–6)	SMA	Natural	2″	$3\farcs08 \times 2\farcs79$, P.A. = 58.9°	0.45	7, 9(c), 9(f)
	ASTE+SMA	Natural	2″	$3\farcs82 \times 3\farcs47$, P.A. = 59.0°	0.30	6, 9(a), 9(e)
		Uniform	3″	$3\farcs83 \times 3\farcs61$, P.A. = 26.9°	0.438	9(b)

constructing the continuum maps. For the line maps, we subtracted the continuum by fitting a linear baseline to the adjacent line-free channels in the visibility data. The continuum maps, as well as the line maps in ^{12}CO(2–1), ^{13}CO(2–1), and C^{18}O(2–1), were made using natural weighting of the visibilities. Line maps in CS(7–6) were made using natural weighting along with tapering to enhance the brightness temperature sensitivity for detecting dim features. Unlike us, Jørgensen et al. (2007) did not apply a tapering to the visibilities when constructing their maps, explaining why their integrated-intensity CS(7–6) map made from the same data is relatively weak and shows no appreciable structure. The angular resolution and rms noise fluctuations of the maps thus produced are summarized in Table 1. In addition, as explained next, the SMA data in CS(7–6) were combined with ASTE data in this line (Section 2.2) to study features on scales larger than are detectable in the SMA maps alone.

2.2. ASTE

We used the ASTE data on L483 taken in 2006 August and previously published by Takakuwa et al. (2007). In the observation, a square area having angular dimensions of $50'' \times 50''$ centered on the protostar was mapped in the CS (7–6) and HCN(4–3) lines simultaneously. The map comprised thirty-four individual pointings, each separated by 10″, compared with an FWHM for the ASTE telescope of 22″. The emission in both lines is spatially extended but confined within the region mapped. In this manuscript, we concern ourselves with the CS(7–6) data only. The channel width used in the observation of CS(7–6) with ASTE was 0.11 km s^{-1}, smaller than that for the same line observed with the SMA as mentioned above.

2.3. Combining SMA and ASTE Data

As a first step toward combining the SMA and ASTE data sets, we resampled the ASTE data in velocity to match the larger channel width of this line in the SMA data. The intensity units of the ASTE data are in antenna temperature, T_A^* (K), which we converted to flux density, S (Jy/beam), using the relationship

$$S = \frac{2k_B\Omega_{\rm beam}}{\lambda^2}\frac{T_A^*}{\eta_{\rm mb}} \quad (1)$$

where k_B is the Boltzmann constant, λ the wavelength, $\Omega_{\rm beam} = 22''$ the solid angle of the ASTE beam, and $\eta_{\rm mb} \sim 0.6$ the main-beam efficiency of the ASTE. We then resampled the ASTE image cube to the primary beam response of the SMA by first deconvolving this image cube with a two-dimensional Gaussian function having an FWHM of 22″ (the ASTE beam) and then multiplying the resultant image cube with a two-dimensional Gaussian function having an FWHM of 36″ (the SMA primary beam). We then applied a Fourier transform to this image cube to produce visibility data. The density of data points in the *uv*-plane for the ASTE data (∼300 data points per *uv*-distance of 1 kλ) was chosen to closely match that of the SMA data.

A common problem encountered when combining data from different telescopes is differences in their absolute flux calibration. When combining single-dish with interferometric data, a standard check is how well the flux densities from the two telescopes agree at the same *uv*-spacings. In the case here, however, there is no overlap in *uv*-space between the ASTE and SMA data. Nevertheless, there is no apparent discontinuity in flux density between the two telescopes in *uv*-space, providing no evidence for a serious discrepancy in their absolute flux calibration (Leung 2015).

Finally, we used the combined ASTE and SMA visibility data to make CS(7–6) channel maps. Like before, we subtracted the continuum by fitting a linear baseline to the adjacent line-free channels in the visibility data. We found tapering to be necessary for suppressing sidelobes that otherwise produced prominent artifacts in the CLEANed maps. The parameters of the combined maps made using natural and uniform weightings, with tapering applied in both weighting schemes, are summarized in Table 1.

3. RESULTS

3.1. Continuum

Figure 1 shows the continuum maps at 1.3 mm and 0.8 mm made with the SMA. From a two-dimensional Gaussian fit to the source detected in the individual maps, we inferred its physical parameters at each wavelength as listed in Table 2. The source is resolved along its major axis only; no useful upper limit could be obtained for its dimension along the minor axis. With a total flux density of 62 ± 6 mJy at 1.3 mm and 98 ± 9 mJy at 0.8 mm, the spectral index, α (defined as $S \propto \nu^{\alpha}$), of the continuum source is 1.1 ± 0.5. This spectral index is much flatter than that expected for dust emission at millimeter and submillimeter wavelengths of, typically, $\alpha \sim 3$ (Beckwith et al. 1990). Our measurements of the source spectral index are likely compromised by having resolved out different amounts of the continuum emission at different wavelengths. The same problem plagues observations of the continuum emission by Jørgensen (2004) using the Owens

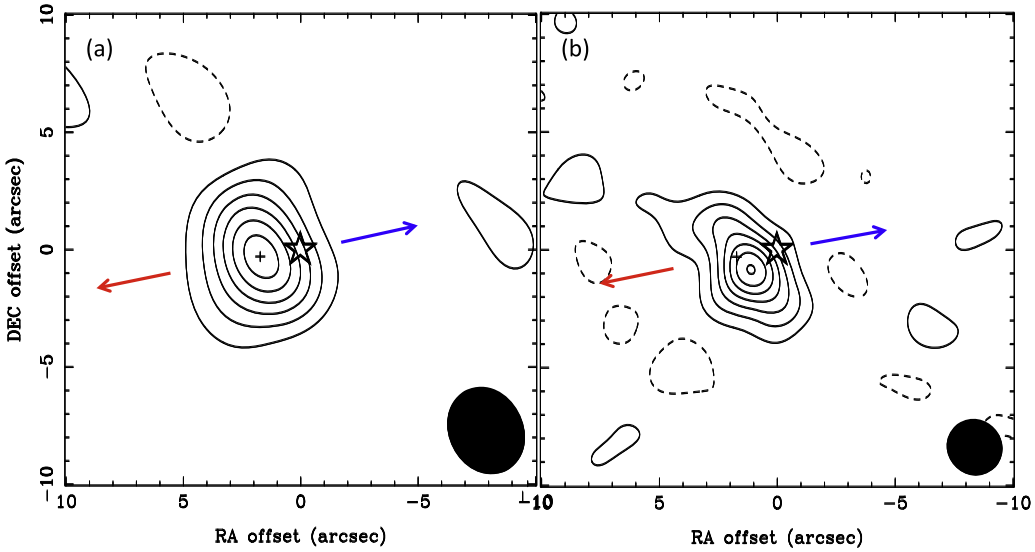

Figure 1. Contours showing continuum emission at (a) 1.3 mm and (b) 0.8 mm. Contour levels are plotted at (a) -2σ, 2σ, 4σ, ..., 12σ and for (b) -2σ, 2σ, 4σ, ..., 14σ, where σ is the rms noise level of the corresponding map; negative levels are indicated by dashed lines, and positive levels by solid lines. The plus sign in each panel marks the centroid of the 1.3 mm continuum, which we take to be the center of the envelope (see text). The same plus sign is shown in the remaining figures where relevant. The star marks the centroid of a radio source at 3.6 cm. The size of the star indicates the $\pm 1\sigma$ positional uncertainty of the 3.6 cm centroid. The arrows show the axis of a bipolar molecular outflow from L483, colored blue for the blueshifted side and red for the redshifted side (see text). The synthesized beam at each wavelength is shown by a black ellipse at the lower right corner of each panel. In this and all the remaining relevant figures, the map parameters (rms noise level and size of the synthesized beam) are listed in Table 1.

Table 2.
Parameters of Continuum Fitting. (R.A., decl.)(J2000) of Protostar Position, Estimated by Beltrán et al. (2001) from 3.6 cm Radio Source, is (18:17:29.86, −04:39:38.80)

Fitting Parameters	1.3 mm	0.8 mm
Peak position R.A.	18:17:29.97 ± 0.″18	18:17:29.94 ± 0.″14
Peak position decl.	−04:39:39.09 ± 0.″22	−04:39:39.56 ± 0.″16
Total flux (mJy)	62 ± 6	98 ± 9
Position angle (deg)	12 ± 16	30 ± 6
Deconvolved size along major axis (arcsec)	2.99 ± 0.5	2.57 ± 0.53

Valley Radio Observatory (OVRO), where the continuum emission at 3.4 mm and 2.7 mm has a measured spectral index of ∼1.75. By contrast, Shirley et al. (2000) reported a higher spectral index of 3.3 ± 0.6 from observations of the continuum at 0.85 mm and 0.45 mm using SCUBA on the JCMT. With an aperture of 40″, they mapped the continuum emission out to a radius of ∼60″, and thus the measured spectral index is not affected by the emission being resolved out differently at different wavelengths.

As mapped at an angular resolution of 7.″9 at 0.45 mm with the JCMT, the dust envelope is elongated approximately along the east–west direction at angular radii of up to ∼30″, in roughly the same direction as a bipolar molecular outflow (outflow axis at a position angle of ∼100°, as indicated by the arrows in Figure 1) from this protostar (see Section 3.2). As mapped at an angular resolution of ∼6″–9″ with OVRO at 3.3 mm and 2.6 mm, Jørgensen (2004) finds that the inner regions of the continuum emission—which can be detected farther out than in our maps—also is elongated in the east–west direction. By comparison, in our maps at a factor of ∼2 higher angular resolution, the major axis of the continuum source has an FWHM of 2.″99 ± 0.″5 and a position angle of 12° ± 16° at 1.3 mm and an FWHM of 2.″57 ± 0.″53 and a position angle of 30° ± 6° at 0.8 mm. Thus, rather than being elongated along the outflow axis, we find the inner regions of the continuum emission to be elongated roughly orthogonal to the outflow axis.

Table 2 lists the centroids of the continuum emission at 1.3 mm and 0.8 mm based on our Gaussian fits. Their positions agree to within 2σ. These positions also agree within 2σ with that of a compact source detected at 3.6 cm by Beltrán et al. (2001) (indicated by a star symbol in Figure 1), attributed to an ionized jet from the protostar. The good agreement between the centroid of the continuum source and the location of the protostar (from its ionized jet) gives us confidence that we have correctly inferred the central position of the envelope. Because the formal position of the continuum centroid at 1.3 mm most closely coincides with the centroid of a compact central component detected in ^{12}CO(2–1) and ^{13}CO(2–1) as described in Section 3.2 and CS(7–6) as described in Section 3.3, we henceforth use this position to define the center of the envelope around L483. The formal position of the continuum centroid at 1.3 mm is marked by a plus sign in Figure 1, as well as in all the relevant figures to follow.

3.2. ^{12}CO(2–1) and ^{13}CO(2–1)

Figure 2 shows the ^{12}CO(2–1) and Figure 3 the ^{13}CO(2–1) channel maps made with the SMA. The corresponding integrated-intensity maps are shown in Figure 4, where the line emission at redshifted velocities is plotted in red contours and that at blueshifted velocities is plotted in blue contours. The integrated-intensity maps are overlaid on a *Spitzer* image that shows bright reflection (scattered light) cavities on the eastern and westerns sides of the center evacuated by a bipolar outflow from the protostar. We do not show the corresponding maps made in C^{18}O(2–1) as this line is weakly detected in just a few channels and does not provide any additional information not readily available from the ^{12}CO(2–1) and ^{13}CO(2–1) maps. Notice that in the channel maps, little or no emission is detected

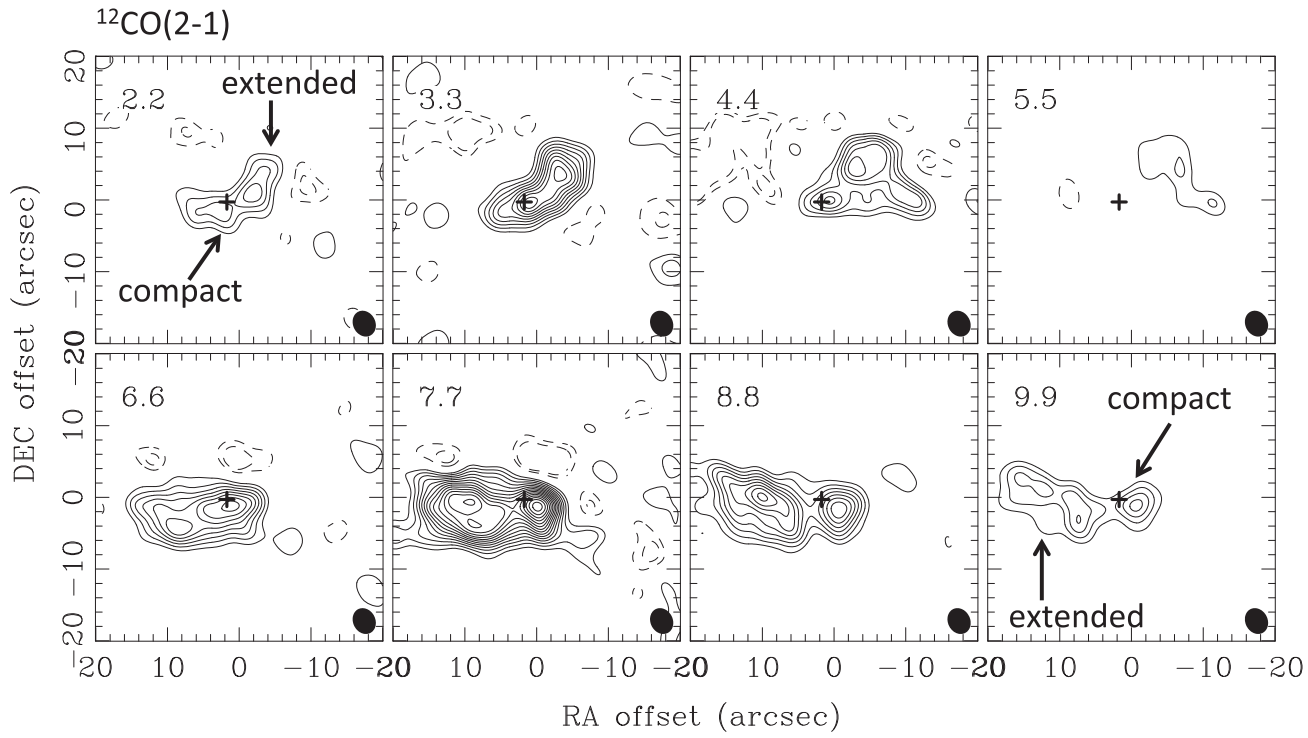

Figure 2. Channel maps in ^{12}CO(2–1) made from archival data taken with the SMA. Contour levels are plotted at -8σ, -5σ, 5σ, 8σ, 11σ, ... , 44σ. In each panel, the plus sign marks the centroid of the 1.3 mm continuum, the channel velocity (in km s^{-1}) is labeled at the top left corner, and the synthesized beam is shown by a black ellipse in the lower right corner. Emission labeled "extended" corresponds to a bipolar molecular outflow from L483, and that labeled "compact" corresponds to a newly discovered compact central component that has a spatial-kinematic structure different from the outflow.

within ~ 1 km s^{-1} of the systematic velocity, which Takakuwa et al. (2007) estimate to be close to 5.6 km s^{-1} based on the overall line profile in HCN(4–3) and CS(7–6) as observed with ASTE (summed over a region $20'' \times 30''$ in size). The emission close to the systemic velocity blends with that from the surrounding molecular cloud and is strongly if not completely resolved out by the interferometer. Away from these velocities, the overall emission in both ^{12}CO(2–1) and ^{13}CO(2–1) is clearly elongated in the east–west direction, as can be seen also in the integrated-intensity maps.

A careful inspection of the channel and integrated-intensity maps reveals that the emission in both ^{12}CO(2–1) and ^{13}CO (2–1) originates from two components, labeled in these maps as "compact" and "extended." These two components exhibit not only different spatial extents but also kinematics. In the channel and integrated-intensity maps of both ^{12}CO(2–1) and ^{13}CO (2–1), the extended component can be seen to be elongated approximately along the east–west direction and to be preferentially blueshifted on the western side and redshifted on the eastern side. This component is therefore elongated along the same direction and exhibits the same direction in velocity gradient as a bipolar molecular outflow mapped by Tafalla et al. (2000) in ^{12}CO(2–1) using the IRAM 30 m telescope and by Velusamy et al. (2014) in ^{12}CO(1–0) using OVRO. In the single-dish map made with the IRAM 30 m telescope, the ^{12}CO(2–1) emission can be traced out to $\sim 50''$ ($\sim$10,000 au) on each side of the protostar. In the interferometric map made with OVRO, the ^{12}CO(1–0) emission can be traced out to a smaller radial extent of $\sim 30''$ (6000 au) and almost completely fills the western cavity but only partially fills the eastern cavity. In the SMA map shown here, both the ^{12}CO (2–1) and ^{13}CO(2–1) emission can be traced out to an even smaller radial extent of $15''$ (3000 au) and almost completely fills the inner region of the eastern cavity but only partially fills the inner region of the western cavity. Evidently, in interferometric maps, the degree to which the CO emission detected fills the outflow cavities depends on the amount of emission recovered.

In the channel maps of both ^{12}CO(2–1) and ^{13}CO(2–1), a compact component can be seen close to the center and lying on the opposite side of the protostar compared with the (bulk of the emission from the) extended component in a given channel. This compact central component produces in large part the blueshifted emission on the western side and the redshifted emission on the eastern side of the center, having an opposite direction in velocity gradient to the extended component. The existence of a compact central component in CO that is spatially and kinematically distinct from the larger-scale bipolar molecular outflow was not previously known or recognized.

Because of their opposite directions in velocity gradients, the compact central and extended components are better separated into different features in position–velocity (PV) diagrams. Figure 5 (upper row) shows the PV diagrams for ^{12}CO(2–1) and ^{13}CO(2–1) along a position angle of 102° through the center. This is the position angle where we find the extended component to exhibit the largest velocity gradient, and is essentially identical to the position angle of $\sim$100° measured by Velusamy et al. (2014) for the axis of the bipolar outflow cavities from their *Spitzer* image. Along this axis, two partially

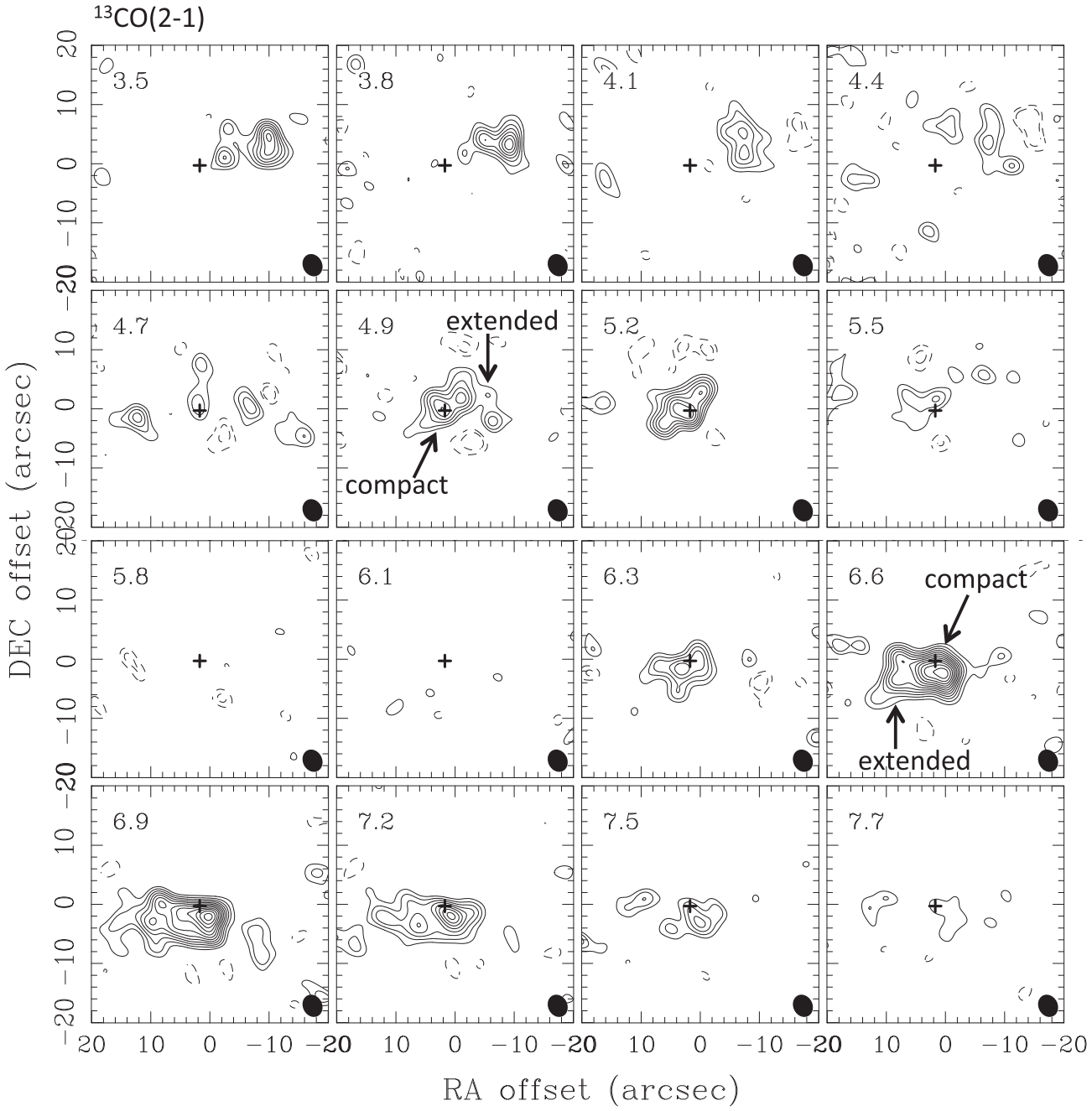

Figure 3. Channel maps in ^{13}CO(2–1) made from archival data taken with the SMA. Contour levels are plotted at -3σ, -2σ, 2σ, 3σ, 4σ, ..., 13σ. Other symbols and labels are the same as in Figure 2.

blended components can be seen in the PV diagrams of both ^{12}CO(2–1) and ^{13}CO(2–1).[5] Not only do these two components have different spatial extents and opposite directions in velocity gradients, but they also have different absolute magnitudes in their velocity gradients. The solid line indicates the approximate velocity gradient of the extended component. The dashed line indicates the velocity gradient of the same compact central component detected in CS(7–6), in which its velocity gradient is more accurately defined, as described next in Section 3.3. As can be seen, the compact central component has a much steeper (and an opposite direction in) velocity gradient (as measured in velocity change per unit length) compared with the extended component.

A visual inspection of the channel and integrated-intensity maps reveals that the compact central component also exhibits a velocity gradient across the outflow axis. This velocity gradient is visually apparent in the ^{12}CO(2–1) channel maps shown in Figure 2, where emission from the compact central component at redshifted velocities of 6.6–9.9 km s^{-1} is clearly displaced to the south relative to its emission at blueshifted velocities of 2.2–4.4 km s^{-1}. Similarly, in the ^{13}CO(2–1) channel maps shown in Figure 3, the emission from the

[5] We tried making maps with different weightings to better resolve out the extended component so as to make the compact central component more discernible. Because the extended component exhibits considerable small-scale structure, however, we could not separate out the compact central component any better using different weighting schemes.

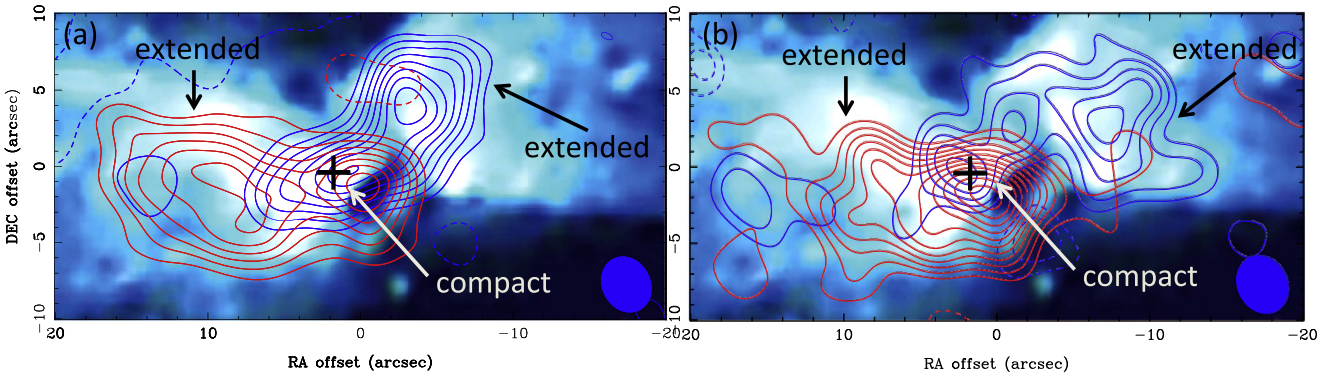

Figure 4. Contours showing integrated intensities in (a) ^{12}CO(2–1) over the velocity range 2.2–4.4 km s^{-1} plotted in blue and 6.6–9.9 km s^{-1} in red; and (b) ^{13}CO (2–1) over the velocity range 3–5.5 km s^{-1}in blue and 6.3–7.5 km s^{-1} in red. Color image shows the bipolar outflow cavities at infrared wavelengths taken by *Spitzer* (Velusamy et al. 2014). Contour levels are plotted at (a) –10σ, 10σ, 16σ, 22σ, 28σ, ... , 52σ, where σ = 0.25 (Jy km s^{-1})/beam; and (b) –4σ, -2σ, 2σ, 4σ, ..., 12σ, where σ = 0.3 (Jy km s^{-1})/beam. Other symbols and labels are the same as in Figure 2.

compact central component at redshifted velocities of 6.6–7.5 km s^{-1} is clearly displaced to the south relative to its emission at blueshifted velocities of 4.7–5.5 km s^{-1}. Figure 5 (lower row) shows the PV diagrams for ^{12}CO(2–1) and ^{13}CO(2–1) along a position angle of 12° (i.e., orthogonal to the outflow axis) passing through the center. A velocity gradient is clearly apparent in ^{13}CO(2–1), such that redshifted emission is displaced southward relative to the blueshifted emission. The PV diagram in ^{12}CO(2–1) also suggests a similar direction in velocity gradient, although not as obvious as in ^{13}CO(2–1). The long-dashed line in these PV diagrams indicates the velocity gradient of the same compact central component detected in CS (7–6) across the outflow axis (Section 3.3). Jørgensen (2004) measured the same direction in velocity gradient for a compact central feature mapped in N_2H^+(1–0), CS(2–1), and HCN(1–0) with the SMA. They suggest that this feature may trace the dense inner region of the rotating envelope.

3.3. CS(7–6)

Figure 6 shows the CS(7–6) channel maps made from the combined ASTE+SMA data, and Figure 7 shows the CS(7–6) channel maps made from the SMA data alone. As we shall demonstrate, just like the emission in ^{12}CO(2–1) and ^{13}CO (2–1), the emission in CS(7–6) is produced by two components having different spatial-kinematic structures. These components are labeled in the channel maps of Figures 6–7 (as well as the other relevant figures to follow) as "extended" (beyond ∼4″) and "compact" (confined within ∼4″). In Figure 6, which shows the combined ASTE+SMA channel maps, the emission over the velocity range 5.0–6.1 km s^{-1} is dominated by the extended component. Beyond this velocity range on both the blueshifted and redshifted sides, the emission is dominated by the compact central component, which therefore extends to a higher radial velocity. In Figure 7, which shows the channel maps made from the SMA data only, the extended component is strongly resolved out so that the compact central component dominates in all channels.

Figure 8(a) shows the integrated intensity of CS(7–6) in contours, made from the ASTE+SMA channel maps, overlaid on the same *Spitzer* image shown in Figure 4. The overall morphology of the CS(7–6) emission in this map is defined by the extended component. The emission is elongated in the east–west direction, where it can be traced out to ∼20″ (∼4000 au) from the center, and spans the entire lateral extent of both outflow cavities. Although the east–west elongation of the CS (7–6) emission is evident from just the ASTE map alone, as found by Takakuwa et al. (2007), the relatively large aspect ratio of this component and its close spatial relationship with the outflow cavities can be clearly seen here for the first time. Notice that on angular scales of up to ∼10″ (∼2000 au) from the center, the intensity distribution is somewhat stronger on the western compared to the eastern side. The emission that gives rise to this asymmetric brightness distribution can be most clearly seen in the ASTE+SMA channel maps over the velocity range 5.4–6.1 km s^{-1}. Beyond ∼10″, however, the intensity distribution appears to be approximately symmetric about the east–west direction. Although the asymmetric intensity distribution of the CS(7–6) emission is evident in the ASTE map alone as presented in Takakuwa et al. (2007) and pointed out by Takakuwa & Kamazaki (2011), the combined ASTE+SMA map reveals that this asymmetry arises from emission on angular scales of up to ∼10″ (∼2000 au) from the center but not that much farther out.

In their observations with the ASTE where only the extended component is resolved, Takakuwa et al. (2007) found that the CS(7–6) emission has a velocity gradient in the opposite direction to that of the bipolar molecular (CO) outflow. In the combined ASTE+SMA map, we find the extended CS(7–6) component to exhibit more complex kinematics than can be discerned from the ASTE map alone, as is the case described above for its asymmetric brightness distribution. At a distance along its major axis beyond ∼10″ (∼2000 au) from the center, this component does not exhibit an apparent velocity gradient. In the channel maps of Figure 6, the CS(7–6) emission spans its largest extent in the east–west direction over the velocity range 5.2–5.9 km s^{-1} (straddling the systemic velocity). In each channel map over this velocity range, the line emission is detectable out to ∼20″ (∼4000 au) both east and west of the center. Figure 8(b) shows the integrated-intensity map of CS (7–6) over this velocity range, where blueshifted emission spanning 5.2–5.4 km s^{-1} is plotted in blue contours and redshifted emission spanning 5.8–5.9 km s^{-1} is plotted in red contours. As is apparent, both the blueshifted and redshifted emissions span the same overall extents in the east–west direction. The PV diagram for CS(7–6) along its major axis (position angle of 102°, same as the outflow axis) passing through the center is shown in Figure 9(a). More than ∼10″ from the center, the emission exhibits no apparent velocity gradient.

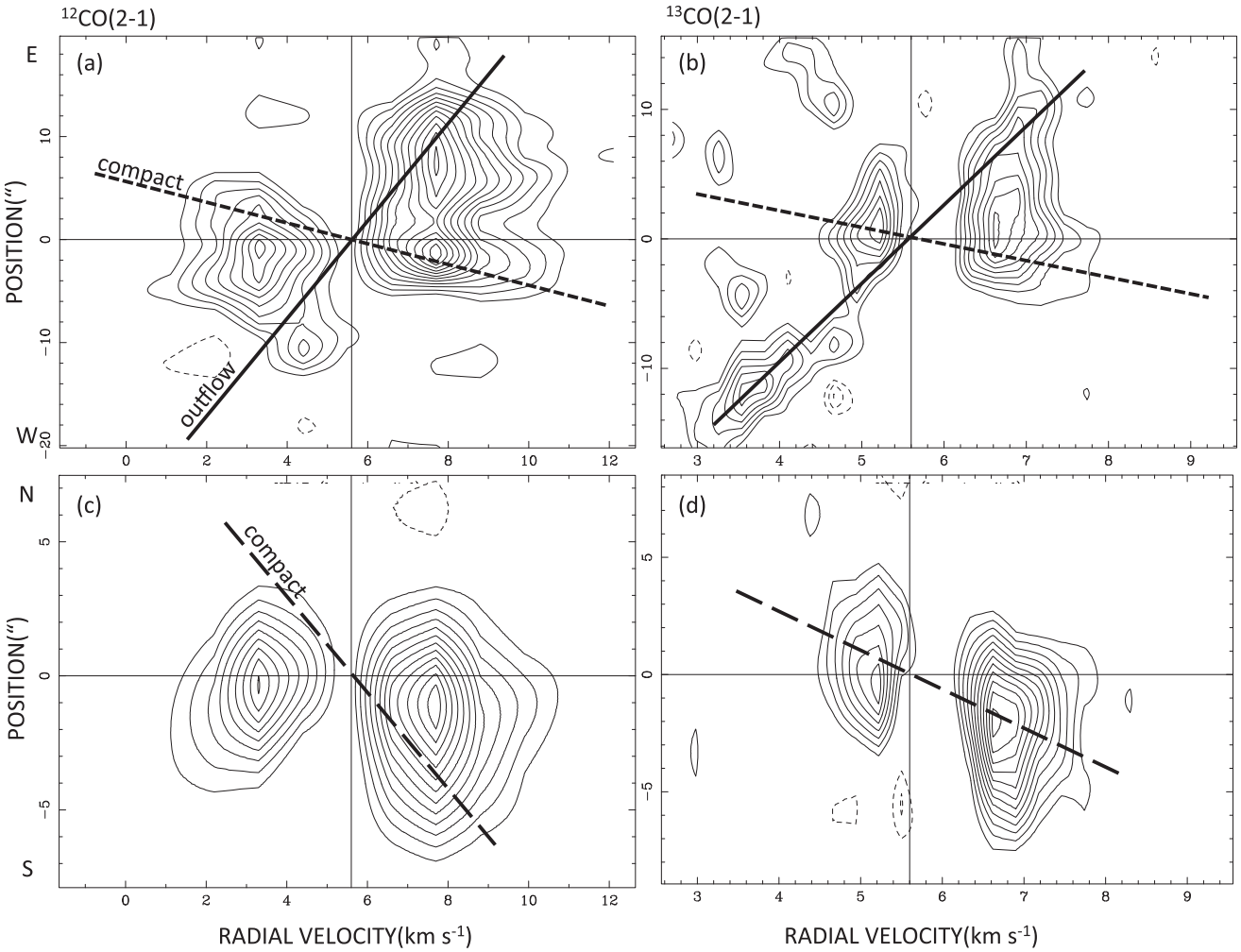

Figure 5. PV diagrams along the outflow axis (P.A. = 102°) in (a) ^{12}CO(2–1) and (b) ^{13}CO(2–1), and the corresponding diagrams across the outflow axis (P.A. = 12°) in (c) ^{12}CO(2–1) and (d) ^{13}CO(2–1). Contour levels for ^{12}CO(2–1) are the same as in Figure 2, and those for ^{13}CO(2–1) are the same as in Figure 3. Solid lines, labeled "outflow," indicate the approximate velocity gradient for the bipolar molecular outflow. Short-dashed and long-dashed lines labeled "compact" indicate, respectively, the velocity gradients of the compact central component along and across the outflow axes. These velocity gradients are inferred not from CO (2–1) but from CS(7–6), as shown in Figure 9. In each panel, the horizontal line indicates the centroid of the 1.3 mm continuum, and the vertical line the systemic velocity.

By contrast, at distances of less than ∼10″ from the center along its major axis, the extended component exhibits a clear velocity gradient. Beyond a velocity range of 5.2–5.9 km s^{-1} in the ASTE+SMA channel maps, the CS(7–6) emission spans a smaller extent in both the eastern and western directions. In these channels, the CS(7–6) emission can be clearly seen to exhibit a velocity gradient along the east–west direction, such that blueshifted emission is stronger on the eastern side and redshift emission stronger on the western side of the center. Figure 8(c) shows an integrated-intensity map of the CS(7–6) emission where blueshifted emission spanning 5.0–5.2 km s^{-1} is plotted in blue contours and redshifted emission spanning 5.8–6.1 km s^{-1} is plotted in red contours. The contour levels plotted have been limited to those that trace emission out to ∼10″ from the center on both its eastern and western sides. Overall, blueshifted emission is stronger to the east and redshifted emission stronger to the west of the center. Evidently, the velocity gradient of the extended CS(7–6) component along its major axis (aligned with the outflow axis) arises from emission extending out to ∼10″ (2000 au) from the center but not farther out. In Figure 9(b), we show a PV diagram in CS(7–6) along the outflow axis as derived from channel maps made using uniform weighting along with tapering of the ASTE+SMA data to help resolve out as well as reduce the sensitivity to emission on relatively large angular scales. The CS(7–6) emission can now be traced out to only ∼15″ on both the eastern and western directions. Over the radial range ∼5″–10″ (∼100–200 au) from the center in both these directions, the emission exhibits a clear velocity gradient with a slope as indicated approximately by the dotted line. For comparison, we also plot in gray contours the PV diagram for ^{13}CO(2–1) along the outflow axis and indicate the approximate velocity gradient of the extended component in this line by the gray solid line. The extended CS(7–6) component has a velocity gradient that is clearly in the opposite direction to that of the extended ^{13}CO(2–1) (and ^{12}CO(2–1)) component.

As mentioned above, the channel maps made from the SMA data alone as presented in Figure 7 preferentially trace a compact central component, although partially blended with emission from the inner regions of the extended component. Figure 8(d) shows the integrated-intensity map in CS(7–6) made from the SMA channel maps, where blueshifted emission is plotted in blue contours and redshifted emission in red contours. The emission at and close to the center is dominated

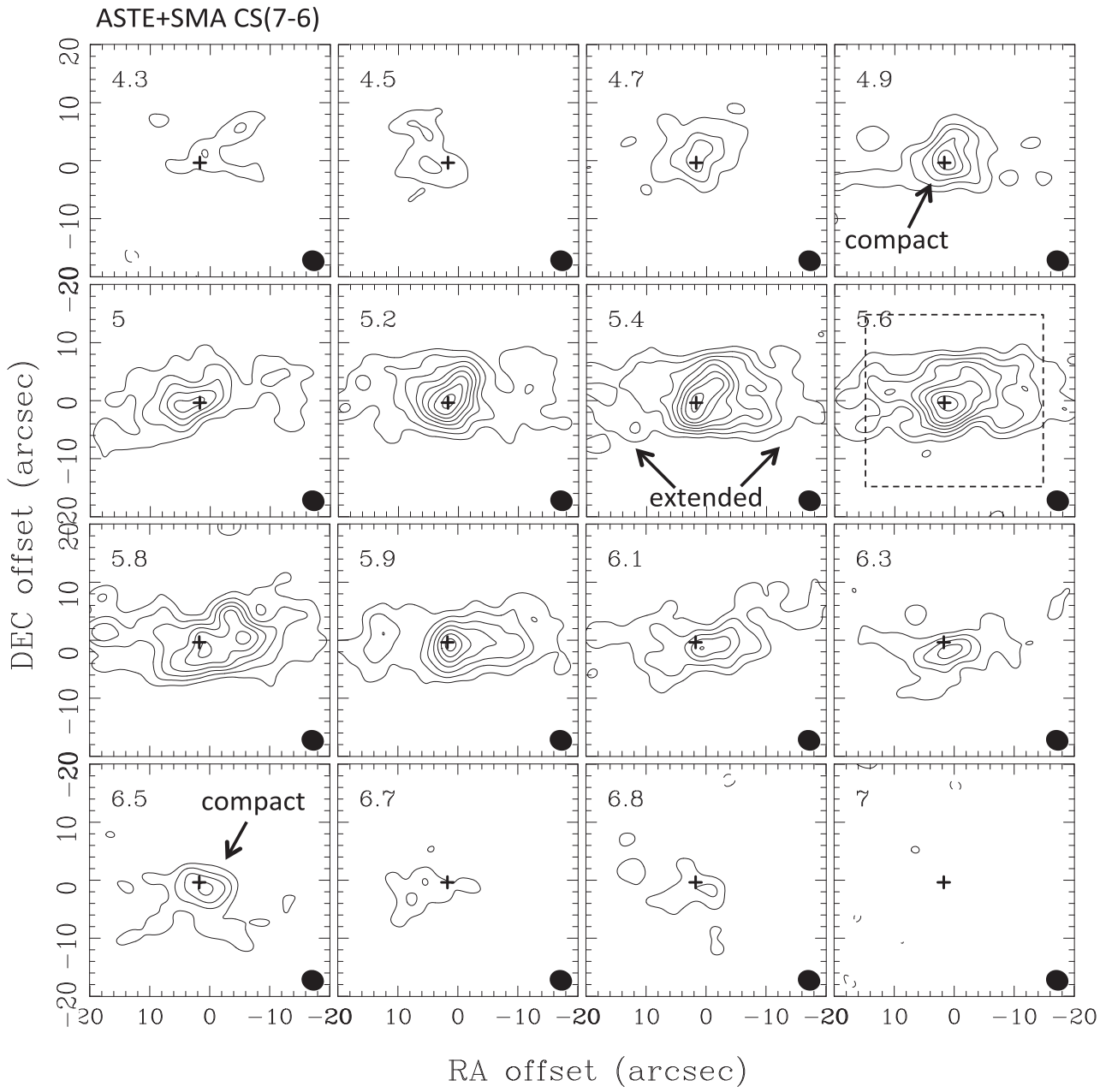

Figure 6. Channel maps in CS(7–6) made by combining archival data taken with the ASTE and the SMA. Contour levels are plotted at 2σ, 4σ, ..., 16σ, where σ is the rms noise level. Emission labeled "extended" and "compact" corresponds to two kinematically distinct components; in this map, the extended component dominates in most of the channels. The square drawn in dashed lines indicates the panel size of Figure 7. Other symbols and labels are the same as in Figure 2.

by the compact central component and exhibits a clear velocity gradient in the north–south direction as well as (albeit less obvious) in the east–west direction. Figure 9(c) shows the PV diagram for CS(7–6) in black contours as measured along the outflow axis. A compact central component confined within a radius of $\sim 4''$ ($\sim$800 au) from the center, comparable to the radial extents of the compact central components in ^{12}CO(2–1) and ^{13}CO(2–1), is apparent with a velocity gradient (slope as indicated by the dashed line) in the same direction but a different magnitude (i.e., steeper velocity gradient) than that of the extended component on intermediate scales (slope indicated, as before, by the dotted line). The PV diagram of Figure 9(c) suggests that the velocity gradient as measured along the outflow axis exhibits an abrupt change rather than a gradual transition between the compact central and extended components. In Figure 9(c), we also plot the PV diagram for ^{13}CO(2–1) along the outflow axis through the center (same as Figure 5) in gray contours. As is apparent, the compact central components in CS(7–6) have similar velocity gradients to the compact central components in ^{12}CO(2–1) and ^{13}CO(2–1).

From their ASTE map, Takakuwa et al. (2007) found that the CS(7–6) emission exhibits a velocity gradient not just along the east–west direction but also along the north-south direction. Such a velocity gradient is readily apparent in the integrated-intensity map of Figure 8(d), where the emission is dominated by the compact central component. As the compact central

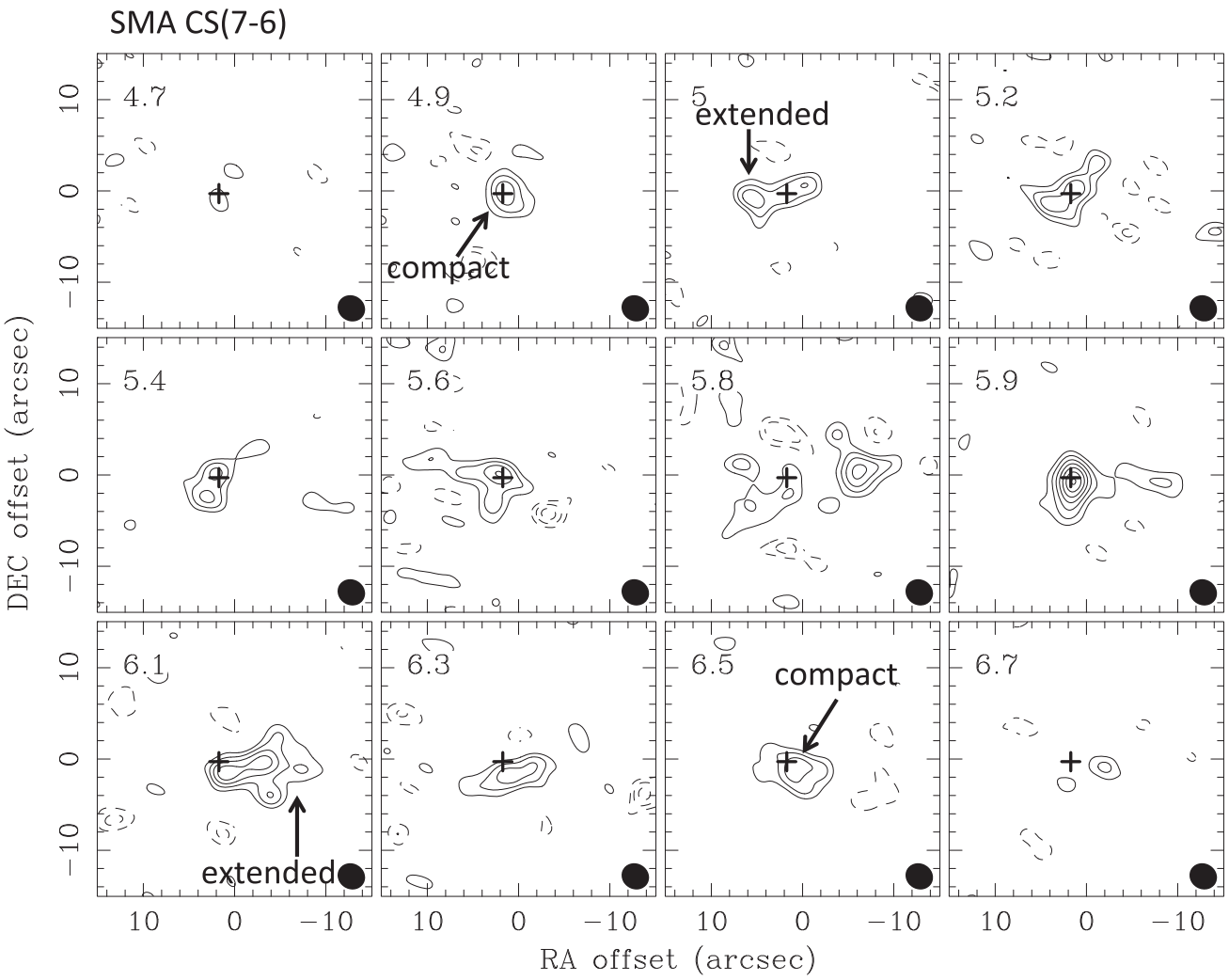

Figure 7. Channel maps in CS(7–6) made from archival data taken with the SMA, highlighting a compact central component. Contour levels are plotted at -3σ, -2σ, 2σ, 3σ, 4σ ..., 8σ, where σ is the rms noise level; negative levels are indicated by dashed lines, and positive levels by solid lines. Other symbols and labels are the same as in Figure 2.

component is much smaller than the ASTE beam, however, the north–south velocity gradient measured in the ASTE map cannot originate from this component, but must instead originate from the extended component. In Figure 10(a), we show in black contours the PV diagram for CS(7–6) across the outflow axis (position angle of 12°) through the center, made from the ASTE+SMA channel maps of Figure 6, which is sensitive to both the extended and compact components. The corresponding PV diagram made from the SMA channel maps of Figure 7, where the emission is dominated by the compact central component, is shown as black contours in Figure 10(b). Both the extended and compact components appear to share a similar velocity gradient across the outflow axis passing through the center. In Figures 10(a)–(b), we also plot in gray contours the PV diagram for ^{13}CO(2–1) across the outflow axis through the center (from Figure 5(d)), where the emission is dominated by the compact central component. The same velocity gradient across the outflow axis through the center is seen in ^{13}CO(2–1) as in CS(7–6). Thus, the compact central component exhibits the same velocity gradients both along and across the outflow axis in CS(7–6) and in ^{13}CO(2–1), and at least in the same direction if not also the same magnitude in ^{12}CO(2–1).

In Figure 8(c), where the extended component defines the overall morphology, the entire CS(7–6) emission is shifted to the north of center at blueshifted velocities and the south of center at redshifted velocities. This behavior suggests a velocity gradient across the outflow axis even at relatively large distances away from the center through the outflow axis. Figure 11 shows PV diagrams made from the ASTE+SMA channel maps cutting across the outflow axis (i.e., along a position angle of 12°) at distances of 3″, 6″, and 9″ (i.e., separation corresponding to the FWHM of the synthesized beam) on opposite sides of the center through the outflow axis. The dashed line drawn in this figure has the same slope as that drawn in Figures 10(a)–(b) for the velocity gradient of both the compact and extended components across the outflow axis through the center. We see that the extended component exhibits an apparently constant velocity gradient across the outflow axis in cuts as far away as ∼6″ to the east and ∼9″ (indeed, we find, as far as ∼10″) to the west of the center through the outflow axis. By contrast, similar cuts across the outflow axis in ^{12}CO(2–1) and ^{13}CO(2–1) do not reveal any discernible velocity gradient except for that through the center, where the velocity gradient is produced by the compact central component.

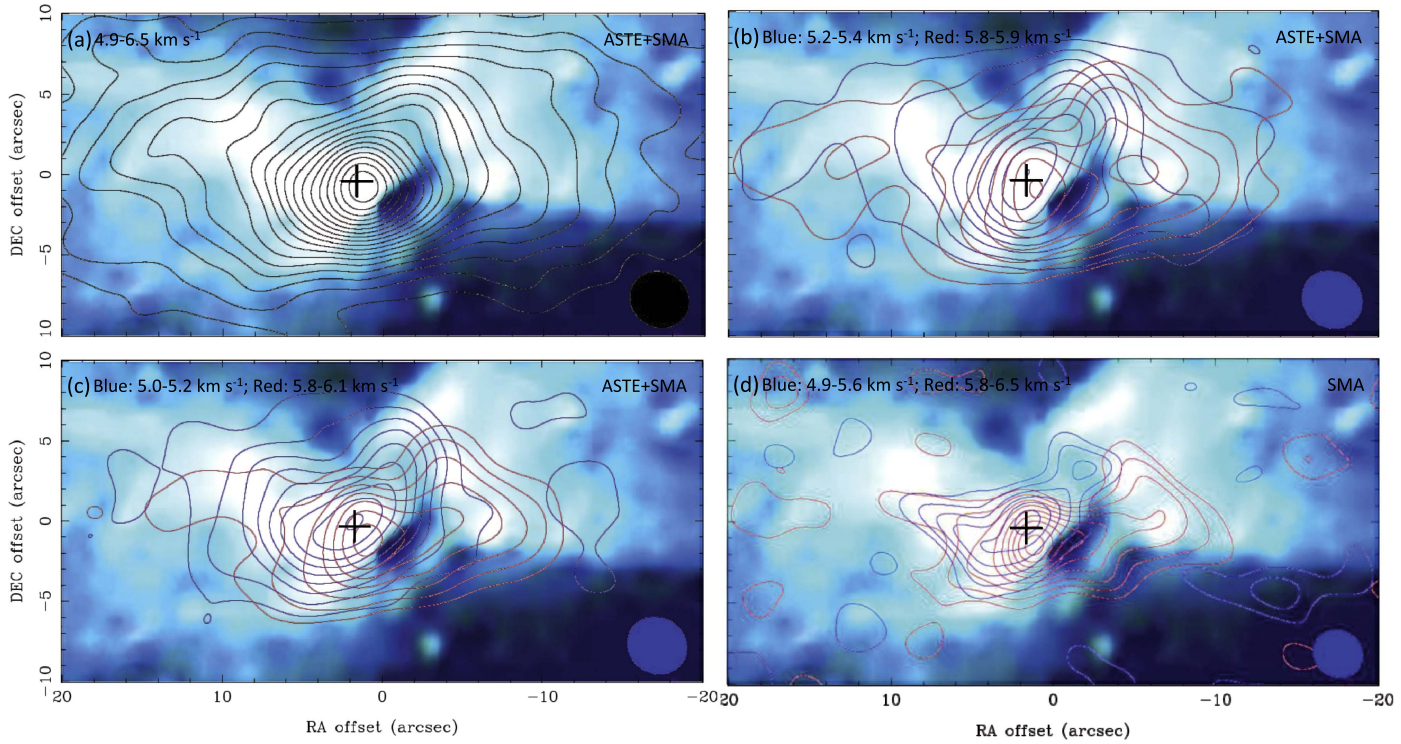

Figure 8. Contours showing the integrated intensities of the combined ASTE+SMA maps in CS(7–6) over the velocity range (a) 4.9–6.5 km s^{-1}; (b) 5.2–5.4 km s^{-1} plotted in blue and 5.8–5.9 km s^{-1} in red; (c) 5.0–5.2 km s^{-1} plotted in blue and 5.8–6.1 km s^{-1} in red; and (d) integrated intensity of the SMA map in CS(7–6) over the velocity range 4.9–5.6 km s^{-1} plotted in blue and 5.8–6.5 km s^{-1} in red. The color image shows the bipolar outflow cavities around L483, the same as that shown in Figure 1. A velocity gradient along the outflow axis (approximately east–west) is only apparent within $\sim$10″ of the center. Contour levels are plotted at (a) 5σ, 10σ, ..., 90σ, where $\sigma = 0.15$ Jy/beam; (b) 2σ, 3σ, ..., 10σ in both red and blue, where $\sigma = 0.3$ Jy/beam; (c) 2σ, 3σ, ..., 10σ in blue and 3σ, 4σ, ..., 10σ in red, where $\sigma = 0.35$ (Jy km s^{-1})/beam; and (d) 2σ, 4σ, ..., 18σ in both red and blue, where $\sigma = 0.12$ (Jy km s^{-1})/beam. The plus sign marks the centroid of the continuum at 1.3 mm.

4. INTERPRETATION

We begin by summarizing the observed properties of the ^{12}CO(2–1), ^{13}CO(2–1), and CS(7–6) emission from L483 that we have to explain. The emission is produced by two spatially and kinematically distinct components—an extended and a compact central component—in each molecular line. The extended component in ^{12}CO(2–1) and ^{13}CO(2–1) is elongated along and has the same direction in velocity gradient as a bipolar molecular outflow from L483 mapped along its entire extent in ^{12}CO(2–1) by Tafalla et al. (2000). This component, which is confined entirely within the pair of outflow cavities seen in scattered light, presumably corresponds to the inner regions of the same bipolar molecular outflow. By contrast, along the outflow axis, the compact central component in ^{12}CO (2–1) and ^{13}CO(2–1) has an opposite direction to and a steeper velocity gradient than the extended component. This component also exhibits a velocity gradient across the outflow axis, seen more clearly in ^{13}CO(2–1) than the more optically thick ^{12}CO(2–1) line.

The extended component in CS(7–6), like the extended component in ^{12}CO(2–1) and ^{13}CO(2–1), also is elongated along the outflow axis, but has a velocity gradient in the opposite direction to the extended ^{12}CO(2–1) and ^{13}CO(2–1) component (and hence also bipolar molecular outflow) along the outflow axis. Its velocity gradient can be detected out to a radial distance of $\sim$10″ (2000 au) from the center but not farther out, similar to the radial extent of its asymmetric brightness distribution (brighter on its redshifted side). The extended CS(7–6) component also exhibits a velocity gradient across the outflow axis, not just through but also away from the center. By comparison, along the outflow axis, the compact central CS(7–6) component has the same direction but a steeper velocity gradient than the extended CS(7–6) component. Across the outflow axis, the compact central CS(7–6) component has the same velocity gradient as the extended CS(7–6) component. Indeed, the compact central components in ^{12}CO(2–1), ^{13}CO(2–1), and CS (7–6) all exhibit a similar direction if not also magnitude in velocity gradient both along and across the outflow axis.

4.1. Bipolar Molecular Outflow

We start by addressing whether, in ^{12}CO(2–1) and ^{13}CO (2–1), the compact central component traces the same bipolar molecular outflow traced by the extended component. Because their velocity gradients have opposite directions, the two lines drawn for their velocity gradients (solid and dashed lines in Figures 5(a)–(b)) take the form of an "X." Such a pattern in velocity gradients is sometimes found for, especially, conical outflow shells having an outflow axis close to the plane of the sky (e.g., see Figures 3 and 5 of Yen et al. (2010) for the bipolar molecular outflow from the protostar B335). If the half-opening angle of the outflow lobe is larger than the inclination of the outflow axis, then for each outflow lobe, one arm of the X traces the shell segment located in front and the other arm the shell segment located behind the plane of the sky. The result is two arms having opposite directions and possibly also different absolute magnitudes (depending on the inclinations of the front and back shell segments of each outflow lobe) in velocity gradients.

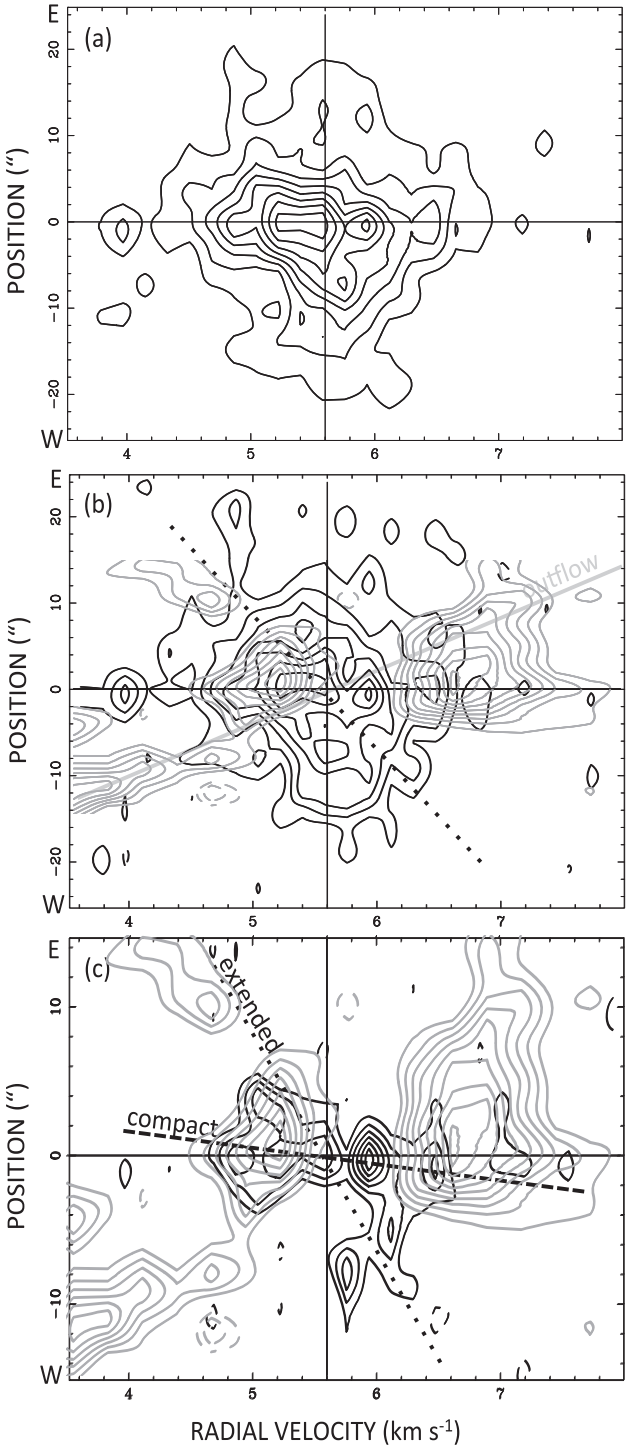

Figure 9. PV diagrams for CS(7–6) in dark contours overlaid on those for ^{13}CO(2–1) in light contours for a cut along the outflow axis (P.A. = 102°). The PV diagrams for CS(7–6) were derived from maps made with (a) ASTE+SMA using natural weighting, dominated by the extended component; (b) ASTE +SMA using uniform weighting, restricting the region of the extended component detectable to within ∼10″ of the center; (c) SMA using natural weighting, dominated by the compact central component. Dotted lines, labeled "extended," indicate the approximate velocity gradient found on intermediate angular scales for the extended component. Short-dashed and long-dashed lines, labeled "compact," indicate, respectively, the velocity gradients of the compact central component along and across the outflow axes. The same lines are drawn in Figure 5. Contour levels are plotted at 2σ, 4σ, ..., 16σ for panels (a) and (b) and at 2σ, 3σ, ..., 10σ for panel (c). Other symbols and labels are the same as in Figure 5.

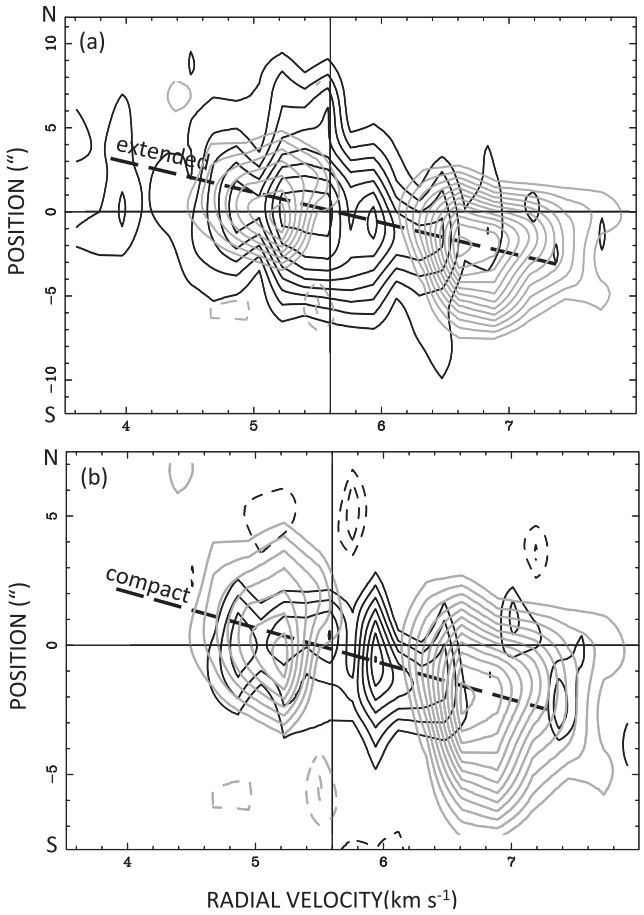

Figure 10. PV diagrams for CS(7–6) in dark contours overlaid on those for ^{13}CO(2–1) in light contours for a cut across the outflow axis (P.A. = 12°). The PV diagrams for CS(7–6) were derived from maps made with (a) ASTE+SMA using natural weighting, dominated by the extended component; and (b) SMA using natural weighting, dominated by the compact central component. Contour levels are plotted at 2σ, 4σ, ..., 16σ. Other symbols and labels are the same as in Figure 5.

In Figure 12(a), we sketch the geometry of the outflow cavities associated with L483. These cavities have a half-opening angle of ∼35°, as measured by Velusamy et al. (2014) from their *Spitzer* mid-IR image, and an inclination for the cavity (and hence outflow) axis of ∼40°, as inferred by Fuller et al. (1995) based on the relative brightness of the bipolar cavities. In this case, because the half-opening angle of the outflow lobe is smaller than the inclination of the outflow axis, both the front and back shell segments of each outflow lobe are predicted to have the same directions in velocity gradients. In PV diagrams, the result is two arms having the same directions but different magnitudes in velocity gradients, incompatible with what we observe in both ^{12}CO(2–1) and ^{13}CO(2–1).

Although the outflow half-opening angle is well defined in the *Spitzer* mid-IR image, it is possible that the inclination of the outflow axis has been incorrectly estimated. Suppose that the outflow inclination angle is larger than estimated (i.e., >55°) so as to assume the geometry sketched in Figure 12(b). Then, the extended component (tracing the shell segment closer to the sky plane) to the east is predicted to be redshifted and that to the west blueshifted, whereas the compact central component (tracing the shell segment farther away from the sky plane) to the east is predicted to be blueshifted and that to the west redshifted, consistent with our observations. Furthermore,

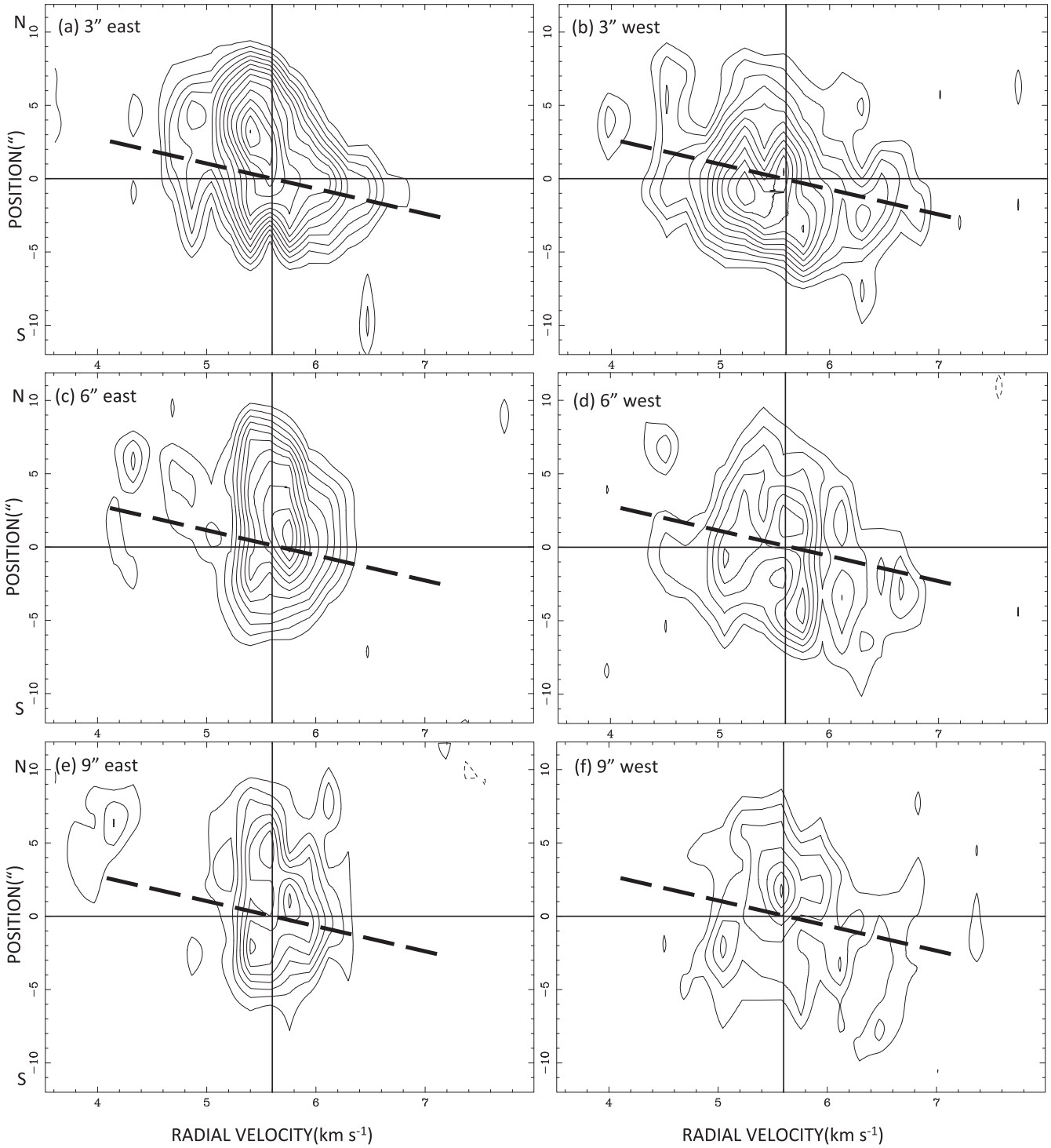

Figure 11. PV diagram for CS(7–6) across the outflow axis (P.A. = 12°) derived from the ASTE+SMA map, dominated by the extended component. The different panels indicate cuts though the outflow axis at different radii from center as labeled in the top left corner. Contour levels are plotted at 2σ, 3σ, ..., 12σ. Long-dashed lines indicate the same velocity gradient as inferred for both the compact and extended components in a cut across the outflow axis through the center as plotted in Figure 9. Other symbols and labels are the same as in Figure 5.

the compact central component should have a steeper velocity gradient than the extended component, again consistent with our observations. This scenario, however, does not explain why the compact central component has a velocity gradient across the outflow axis (not seen in the extended component). Instead, the similar velocity gradients of the compact central components in ^{12}CO(2–1), ^{13}CO(2–1), and CS(7–6) both along and across the outflow axis indicate that they all trace the same feature, different from the bipolar molecular outflow.

4.2. Inflow and Rotation along Cavity Walls

In Figure 13(a), we sketch the inferred geometry of the outflow cavities around L483 (i.e., same as Figure 12(a)) and

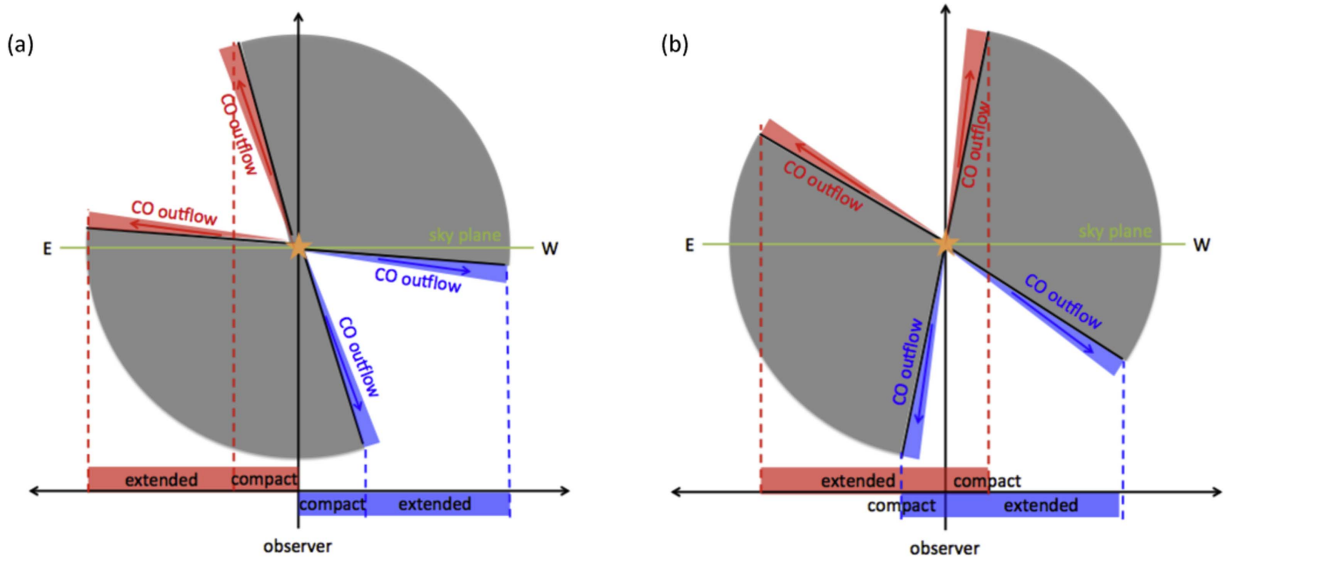

Figure 12. Schematic diagrams showing models for the CO(2–1) emission, demonstrating how a bipolar molecular outflow can possibly give rise to both an extended and a compact central component under (a) the previously inferred geometry of L483 and (b) a modified geometry. The observer is located at the bottom of each diagram, with the solid black arrow indicating the line of sight. The red and blue shaded regions indicate, respectively, the redshifted and blueshifted portions of the bipolar molecular outflow. The rectangular slab at the bottom of each diagram indicates the projected extents and direction in velocity gradients predicted by the model for the compact central and extended components.

indicate inflow along these cavity walls. Large-scale infall of the envelope around L483 has been inferred by Mardones et al. (1997) based on a stronger blueshift asymmetry in single-dish spectra of the optically thick H_2CO(2–1) and CS(2–1) lines and the optically thin N_2H^+(1–0) line. The bipolar molecular outflow may comprise conical shells, but as we shall show, our model does not depend on the exact morphology of this outflow. We also indicate in this sketch the rotation of the envelope as inferred by Jørgensen (2004) from observations in N_2H^+(1–0) and CS(2–1), both of which trace the inner region of the envelope within an angular radius of $\sim 10''$ from the center.

The model sketched in Figure 13(a) can explain, in a qualitative manner, all the features seen in ^{12}CO(2–1), ^{13}CO (2–1), and CS(7–6). In this model, the inflowing cavity walls, possibly elevated in density through compression by the bipolar outflow and heated to higher temperatures by both shocks from the bipolar outflow and radiation from the protostar (a point we shall return to shortly), emit more strongly in molecular lines than the inner cooler regions of the envelope (i.e., toward the midplane). The near and far cavity walls of each outflow lobe have very different sizes as projected in the sky, giving rise to extended (tracing the cavity walls closer to the sky plane) and compact central (tracing the cavity walls farther from the sky plane) components. For an observed angular radius of $\sim 20''$ along the outflow axis for the extended CS(7–6) component, the compact central component is predicted to have an angular radius of $\sim 5''$ along the outflow axis, closely comparable with the radial extent observed for this component in CS(7–6) of $\lesssim 4''$. Both the compact central and extended components are predicted to have an opposite direction in velocity gradient to the bipolar molecular outflow, in agreement with the observations. Furthermore, the compact central component should exhibit a steeper velocity gradient than the extended component, again in agreement with the observations. As mentioned in Section 3.3, the extended component exhibits a velocity gradient along the outflow axis that decreases in magnitude outward, so that no velocity gradient is apparent beyond a radius of $\sim 10''$ (2000 au). This behavior is qualitatively consistent with that expected for infall, where the infall speed increases with decreasing distance from the protostar. We have tried fitting free-fall curves to the PV diagrams shown in Figure 9 (see Leung 2015). Although we can easily find free-fall curves contained within the emitting region, the quality of the data is not sufficient to investigate the radial dependence in the infall speed. Finally, the central continuum source may preferentially trace dust in the midplane of the envelope, explaining why this source is elongated perpendicular to the outflow axis.

As mentioned in Section 1, Takakuwa & Kamazaki (2011) propose that the CS(7–6) emission of L483 as mapped with ASTE is produced by relatively dense and warm gas lifted from the cavity walls and driven outward, as illustrated in Figure 13(b). In this case, for the inferred cavity geometry, both the extended (tracing the cavity walls closer to the sky plane) and compact central (tracing the cavity walls farther from the sky plane) components in CS(7–6) should have velocity gradients in the same direction as the bipolar molecular outflow, in contradiction with our observations. To be more consistent with the observations, the inclination of the outflow axis is required to be smaller (alternatively, the opening angle of the outflow cavity to be larger) so as to produce the cavity geometry sketched in Figure 13(c). With this geometry, the extended CS(7–6) component now has an opposite direction in velocity gradient to the bipolar molecular outflow. The compact central CS(7–6) component, however, still has the same direction in velocity gradient as the bipolar molecular outflow, in contradiction with our observations. A model in which both the compact and extended CS(7–6) components arise from gas dispersed along the cavity walls is untenable.

The extended CS(7–6) component can be detected to a radial velocity of only ~ 0.6 km s^{-1} from the systemic velocity. In both ^{12}CO(2–1) and ^{13}CO(2–1), the emission at such radial

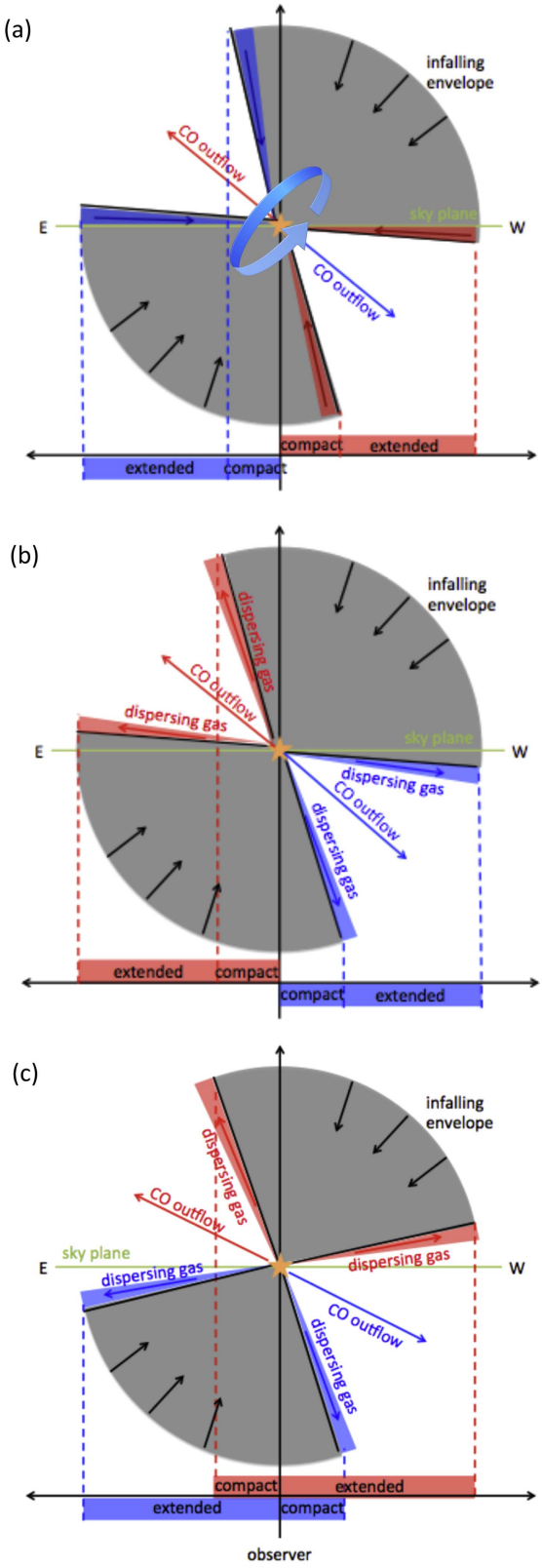

Figure 13. Schematic diagrams showing how the compact central and extended components observed in CS(7–6) for L483 might be produced, by (a) infalling gas along the surfaces of an envelope carved out by a bipolar molecular outflow, as we propose; and by (b and c) gas driven outward from the surfaces of an envelope carved out by a bipolar molecular outflow, as proposed by Takakuwa & Kamazaki (2011), under the inferred geometry and a modified geometry, repectively. Only the model in panel (a) predicts the observed directions in velocity gradients for both the compact central and extended components.

velocities is blended with that of the ambient molecular cloud (which emits strongly in both ^{12}CO(2–1) and ^{13}CO(2–1) but not CS(7–6)) and resolved out by the interferometer, explaining why we do not detect a counterpart to the extended CS(7–6) component in both these lines. By contrast, the compact central component can be detected to a radial velocity as high as $\sim$2.0 km s^{-1} from the systemic velocity, allowing this component also to be detected in ^{12}CO(2–1) and ^{13}CO(2–1) at radial velocities sufficiently removed from the systemic velocity.

The rotation of the envelope naturally explains the similar velocity gradients of the compact central and extended components across the outflow axis. To preserve an approximately constant velocity gradient across the outflow axis at radial distances out to $\sim$10″ from the center, the envelope is required to rotate approximately as a solid body (indicating the efficient outward transfer of angular momentum) out to a radius of $\sim$9″ ($\sim$1800 au) along the equatorial plane (computed for the geometry of the outflow cavity as described above). We note that the asymmetric intensity distribution of the CS(7–6) emission, stronger to the west than the east, can explain why a velocity gradient is detectable in the extended component out to $\sim$10″ to the west but only up to $\sim$6″ to the east of the center across the outflow axis. The asymmetric brightness distribution of the extended CS(7–6) component along its major axis, detectable out to $\sim$10″ from the center, can be attributed to stronger absorption by the cooler part of the envelope (i.e., closer to the midplane) that lies to the foreground of the extended component on the eastern (but not western) side of the center, as previously demonstrated by Takakuwa & Kamazaki (2011). Farther from the center, the gas density and/or temperature presumably drops to a level below which absorption in CS(7–6) is no longer appreciable, thus explaining the apparently symmetric distribution of the extended component along its major axis beyond $\sim$10″ from the center.

Normally, one would not expect to detect bright CS(7–6) emission at radii of up to several thousand au from a low-mass protostar. Here, for illustration, we use the non-LTE 1D radiative transfer code RADEX (van der Tak et al. 2007) to estimate the required temperature and density of the CS gas so as to emit at the observed brightness temperature of $\sim$0.94 K at a distance of 4000 au from the protostar (along the outflow axis). Adopting a CS abundance of $X_{\rm CS} \sim 6.8 \times 10^{-10}$ (derived from the line intensities of multiple CS transitions by Jørgensen et al. 2004) and assuming that the CS(7–6) emission originates from a surface layer of the cavity walls with a depth of between $\sim$100 and $\sim$1000 au, we find a required temperature of $\gtrsim$50 K for a density of $\sim 10^6$ cm^{-3}, or a required density of $\gtrsim 10^7$ cm^{-3} for a temperature of $\sim$10 K. By comparison, in the theoretical model by Masunaga & Inutsuka (2000) for a collapsing core having an initial mass of 1 $M_\odot$, by the time a protostar forms, the density has fallen to $\sim 10^4$–10^5 cm^{-3} and the temperature to $\sim$10 K at a radial distance of $\sim$4000 au. In theoretical simulations, Machida et al. (2014) find that the density of the cavity walls can be significantly elevated (by a factor of several) through compression by a bipolar outflow. In theoretical simulations where the envelope is excavated by a bipolar outflow, Whitney et al. (2003) find that the temperature of the cavity walls can be significantly elevated by irradiation from the protostar. For a protostellar luminosity of $\sim$1 $L_\odot$, they find that the cavity walls can be elevated to a temperature of $\sim$50 K at a radial distance of $\sim$1000 au and $\sim$20 K at a radial distance of $\sim$4000 au (compared with an

ambient temperature of ∼10 K). The protostar in L483 has an order-of-magnitude higher luminosity of ∼9 $L_{\odot}$ (Jørgensen 2004), resulting in an even higher temperature for the cavity walls over the same radial distances. In addition, we note that shocks due to compression by the bipolar outflow also can heat the cavity walls (e.g., van Kempen et al. 2010; Visser et al. 2012). Whether all these processes can produce the required enhancement in temperature and, especially, density for CS(7–6) to be emitted as its observed brightness temperature so far out in the envelope, however, remains to be seen.

5. DISCUSSION

Our new model that offers a full qualitative explanation for the observed CS(7–6) emission, as well as ^{12}CO(2–1) and ^{13}CO(2–1) emission, from L483 requires infalling rather than outflowing gas along the outflow cavity walls of a rotating envelope. We now examine whether our model for L483 can be applied to other protostars that also show extended CS(7–6) emission. These protostars can have different opening angles for their outflow cavities and also be viewed at different orientations, resulting in different observable properties for their CS(7–6) emission. At the present time, apart from L483, the only other protostars for which combined single-dish and interferometer data in CS(7–6) are available are those for L1551 IRS5 and B335, the two objects discussed below.

5.1. L1551 IRS5

L1551 IRS5, a binary protostellar system (see Lim et al. 2016), also exhibits a compact central component in CS(7–6) having a projected radius of ∼400 au (Chou et al. 2014), together with an extended component that is elongated along the outflow axis and detectable out to a projected radius of ∼2500 au (Takakuwa & Kamazaki 2011). Both these components share a number of features in common with the corresponding components around L483. First, the extended CS(7–6) component is brighter on its redshifted side and exhibits a velocity gradient in the opposite direction to that of the bipolar CO outflow. Second, both the compact central and extended CS(7–6) components exhibit a velocity gradient across the outflow axis. By making cuts across the outflow axis in the combined ASTE+SMA maps presented by Takakuwa & Kamazaki (2011), we found that the extended component exhibits a velocity gradient across the outflow axis out to a projected radius of ∼1200 au from the center through the outflow axis (Leung 2015). In addition, throughout the entire extent of the extended CS(7–6) component where a velocity gradient across the outflow axis is detectable, the magnitude of this velocity gradient shows no appreciable change with radius from the center through the outflow axis. Finally, as far as we are aware, no velocity gradient has ever been reported for cuts across the axis of the bipolar molecular outflow of L1551 IRS5 as traced in CO. The singular difference is that, unlike L483, the compact central CS(7–6) component exhibits a velocity gradient in the opposite direction to that of the extended CS (7–6) component, and hence the same direction in velocity gradient as the bipolar CO outflow.

As with other protostars, Takakuwa & Kamazaki (2011) attributed the extended CS(7–6) component in L1551 IRS5 to gas lifted from the outflow cavity walls and dispersed outward. Both Takakuwa & Kamazaki (2011) and Chou et al. (2014) attribute the compact central CS(7–6) component to the inner region of a flattened, rotating, and infalling envelope (i.e., pseudodisk). Again, whether the proposed model is consistent with the observations depends on both the cavity geometry and the viewing angle.

From a *Spitzer* near-IR image of the bipolar cavities, Velusamy et al. (2014) estimate an opening angle of 105° at the base of the outflow cavity associated with L1551 IRS5. Because the walls of the outflow cavities are curved, however, the opening angle of the outflow cavity as measured at the radius of the extended CS emission is somewhat smaller; we estimate ∼90°–100° from the same *Spitzer* image. The inclination of the cavity or outflow axis is not well determined. Based on the radial compared with the tranverse velocities of Herbig–Haro objects associated with the visible jets, Pyo et al. (2002) infer an inclination of ∼45° for the outflow axis. Using the same technique for optical knots in the northern jet, Hartigan et al. (2000) infer an inclination for the outflow axis as large as ∼55°. Other estimates for the inclination of the outflow axis are based on the assumption that this axis is perpendicular to the major axis of the flattened envelope around L1551 IRS5, giving a value of 26° (Momose et al. 1998), or perpendicular to the major axes of circumstellar disks of the binary components, giving values of ∼30° (Lim & Takakuwa 2006) and improved values in the range of ∼44°–48° (Lim et al. 2016). The inferred half-opening angle of the outflow cavity around L1551 IRS5 in the range of ∼45°–50° therefore spans a similar range to the arguably more reliable estimates for the inclination of the outflow axis in the range of ∼45°–55°.

In Figure 14(a), we sketch an outflow cavity having a half-opening angle that is smaller than the inclination of the outflow axis to the sky plane. Note that, for a given outflow cavity, the far side of the cavity wall lies on the opposite side of the center compared with the near side. Just like in our model for L483, in Figure 14(a) material in the cavity walls is inflowing, in keeping with the infalling motion inferred for the envelope of L1551 IRS5 (Momose et al. 1998). This model predicts an extended component tracing the cavity wall nearer the sky plane that has an opposite direction in velocity gradient to the bipolar molecular outflow, but a compact central component tracing the cavity wall farther from the sky plane that has the same direction in velocity gradient as the bipolar molecular outflow, consistent with the observations. Furthermore, the extended CS(7–6) emission on the redshifted outflow side is subject to foreground absorption by the envelope, explaining why this emission is stronger on its redshifted compared with its blueshifted side. We note the alternative model proposed by Takakuwa & Kamazaki (2011) and Chou et al. (2014) also can explain the kinematics of the compact central and extended CS(7–6) components provided that the outflow cavity has a half-opening angle larger (rather than, in our model, smaller) than the inclination of the outflow axis to the sky plane.

In Figure 5 of Chou et al. (2014), the integrated-intensity map in CS(7–6) close to the systemic velocity (spanning the velocity range 5.6–7.8 km s^{-1}) shows an approximately circular structure. Chou et al. (2014) attribute this structure to an inclined pseudodisk (emission at higher velocities is attributed primarily to a circumbinary disk). Rather than being strongly elongated perpendicular to the outflow axis as would be expected for an inclined pseudodisk, however, the observed structure appears to have similar extents along as well as across the outflow axis. The model shown in Figure 14(a) predicts that

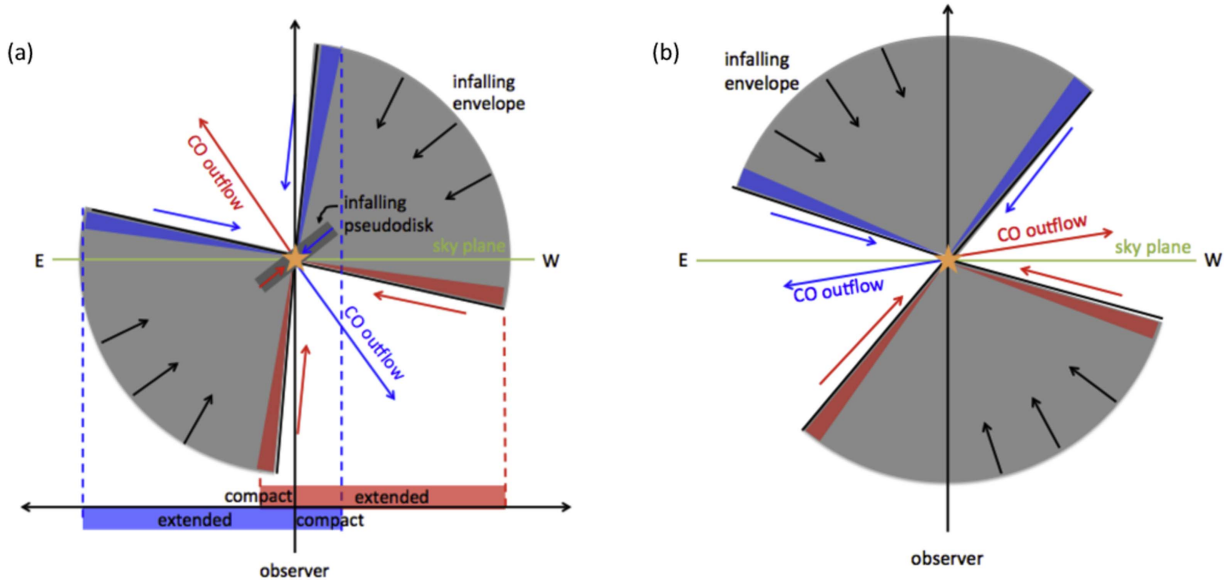

Figure 14. Schematic diagrams showing how the compact central and extended components observed in CS(7–6) can be produced by infalling gas along the surfaces of an envelope carved out by a bipolar molecular outflow, as we propose, for (a) L1551 IRS 5 and (b) B335.

the cavity walls aligned nearly along the line of sight should produce a compact central component that is elongated along the outflow axis. Thus, in L1551 IRS5, both the cavity walls aligned close to the line of sight and a pseudodisk could contribute to its compact central CS(7–6) emission. Both features would produce emission along the outflow axis having the same direction in velocity gradients and thus be difficult to separate.

The extended CS(7–6) component is detectable to a radial velocity of only $\sim$0.5 km s^{-1} from the systemic on both its blueshifted and redshifted sides. In CO, emission over this velocity range is resolved out in interferometric maps, explaining why—as in L483—we do not see CO emission from the cavity walls closer to the sky plane. The compact CS component is detectable to a velocity of $\sim$2.5 km s^{-1} from the systemic on both its blueshifted and redshifted sides. Emission in CO beyond $\sim$1 km s^{-1} from the systemic is not resolved out, and so the envelope surfaces close to the sightline should also give rise to a compact central CO component, just like in L483. Indeed, an inspection of the ^{12}CO(2–1) map of L1551 IRS5 made by Wu et al. (2009) at a high angular resolution with the SMA reveals a compact central component of size $\sim$800 au extended along the outflow direction. This component has a velocity gradient in the same direction and with a comparable magnitude as the compact central CS(7–6) component. Wu et al. (2009) attribute the compact central component detected in ^{12}CO(2–1) to material recently entrained by the jets from the binary system in L1551 IRS5. Instead, in our model, this component corresponds to the same compact central component detected in CS(7–6) originating from the infalling cavity walls.

5.2. B335

B335 is a single Class 0 protostar. It exhibits extended CS(7–6) emission that is elongated along the outflow axis just like in L483 and L1551 IRS5, and which is detectable out to a projected radius of $\sim$2000 au from the protostar (Yen et al. 2011). Both blueshifted and redshifted emission is detected on both sides of the protostar along the outflow axis over nearly the entire range of radial velocities where CS(7–6) emission is detectable. Nevertheless, the redshifted emission reaches higher radial velocities on the eastern side and the blueshifted emission higher radial velocities on the western side of the protostar (see Figure 9 of Yen et al. 2011), giving rise to a velocity gradient in the opposite direction to that of the bipolar molecular outflow just like the extended CS(7–6) component in L483 and L1551 IRS5. In the ASTE map of B335 made by Takakuwa et al. (2007), the extended CS emission exhibits a velocity gradient across the outflow axis cutting through the protostar. In the ASTE+SMA map presented by Yen et al. (2010), however, there is no clear velocity gradient across the outflow axis cutting through the protostar (see their Figure 9, right panel). We have made PV diagrams from the ASTE+SMA map presented by Yen et al. (2011) cutting across the outflow axis at different radial distances from the center through the outflow axis. The PV diagrams for some of these cuts suggest a velocity gradient in the same direction as that seen in the ASTE map, whereas others show no appreciable velocity gradient. Unlike L483 and L1551 IRS5, however, B335 does not exhibit a distinct compact central component.

The bipolar molecular outflow from B335 has its major axis along the east–west direction and is closely aligned to the plane of the sky (Yen et al. 2010). Based on the relative masses deduced for the blueshifted and redshifted portion of each outflow lobe, Hirano et al. (1988) infer an inclination for the outflow axis of $\sim$10°. From *Spitzer* images of the outflow cavities around B335, Velusamy et al. (2014) infer an opening angle for both outflow cavities of $\sim$63°.

Figure 14(b) shows a sketch of the inferred cavity geometry for B335. Like in our models for L483 and L1551 IRS5, material in the cavity walls is inflowing, in keeping with the infalling motion of the envelope (see Yen et al. 2010, and references therein). For B335, both the near and far sides of the cavity walls are foreshortened in projection by nearly comparable amounts, so that one side of the envelope surface extends just a little farther out than the other. Thus, this model does not predict the presence of a compact central component

in CS(7–6), consistent with the observations. Instead, both the near and far sides of the cavity walls should contribute to the extended component on either sides of the center, thus producing both redshifted and blueshifted velocities on either sides of the center, as is observed. Although the near and far sides of the cavity walls have nearly comparable radial extents, for the inferred geometry these two sides have radial velocities that differ by nearly a factor of 2. Thus, along a given line of sight toward the outflow axis, the cavity wall farther from the sky plane should have a higher radial velocity than the cavity wall closer to the sky plane and thus produce a velocity gradient in the opposite direction to the bipolar molecular outflow, as is observed. By contrast, for gas dispersed along the cavity walls, the CS(7–6) emission is predicted to have a velocity gradient in the same direction as the bulk of the bipolar molecular outflow, in contradiction with the observations. Finally, because emission from the walls of both outflow cavities has to propagate through the deeper and hence cooler regions of the envelope in front of the sky plane, the CS(7–6) emission should be approximately equally bright on both sides of the protostar, as is indeed observed.

Finally, we note that the CS(7–6) emission can be traced to a velocity of only $\sim$1 km s^{-1} from the systemic velocities. Over this range of velocities, any corresponding ^{12}CO emission would be blended with that of the surrounding ambient cloud and resolved out by an interferometer.

6. SUMMARY

Single-dish observations of both Class 0 and I sources by Takakuwa et al. (2007) and Takakuwa & Kamazaki (2011) with the ASTE have revealed that their CS(7–6) and HCN(4–3) emissions are elongated along the outflow axis and exhibit a velocity gradient in the opposite direction to that of their bipolar CO outflow. Takakuwa & Kamazaki (2011) propose that these emissions are produced by relatively dense and warm gas flowing outward along the cavity walls evacuated in the protostellar envelope by a bipolar outflow, as might be expected if a wide-angle wind driven from the circumstellar disk of the protostar disperses its envelope. This model requires a particular geometry for the inclination of the outflow axis compared with the opening angle of the outflow cavity and makes definitive predictions about the spatial-kinematic structure of the emission from the hypothesized outflowing gas that can be readily tested.

To study in greater detail the CS(7–6) emission from the protostar L483, we combined previously published single-dish (from the ASTE; Takakuwa et al. 2007) and interferometric (from the SMA; Jørgensen et al. 2007) data for this object. Our maps probe the spatial-kinematic structure of its CS(7–6) emission over a broad range of projected spatial scales from about 600 to 4000 au and reveal new features not previously known or recognized. We find two kinematically distinct components exhibiting the following features:

1. The more extended component, corresponding to that detected with the ASTE by Takakuwa et al. (2007), is highly elongated along the outflow axis and can be traced out to $\sim$20″ (projected distance of $\sim$4000 au) from the protostar. Across the outflow axis, this component appears to fill the lateral extents of the outflow cavities. Despite having a morphology resembling that of the bipolar CO outflow from this protostar, we confirm that the extended component has a velocity gradient in the opposite direction to this outflow as pointed out by Takakuwa et al. (2007).
2. Along the outflow axis, the extended component exhibits a detectable velocity gradient out to a radius of $\sim$10″ ($\sim$2000 au), but not beyond to its outermost detectable extent of $\sim$20″.
3. As previously found by Takakuwa et al. (2007) in their observation with ASTE, the extended component is brighter on the redshifted than its blueshifted side. From the combined ASTE+SMA map, we find that this asymmetric brightness distribution originates from within a radius of $\sim$10″ ($\sim$2000 au). Farther out, the extended component appears to be equally bright on both sides.
4. The newly discovered, more compact central component is confined within a radius of $\sim$4″ ($\sim$800 au). Along the outflow axis, it exhibits a velocity gradient in the same direction as but steeper than that of the extended component.
5. Across the outflow axis, both the compact central and extended components exhibit a similar velocity gradient through the center. Furthermore, the same velocity gradient across the outflow axis can be detected in the extended component as far out as $\sim$6″ ($\sim$1200 au) on the dimmer eastern side and $\sim$10″ ($\sim$2000 au) on the brighter western side of the center through the outflow axis.

From a reanalysis of ^{12}CO(2–1) and ^{13}CO(2–1) maps made with the SMA, we find that these lines also show two kinematically distinct components:

1. The more extended component corresponds to the previously known bipolar CO outflow;
2. The newly discovered, more compact central component is confined within a radius of $\sim$5″ ($\sim$1000 au) and exhibits a velocity gradient in the opposite direction to the extended component (bipolar CO outflow). Both along and across the outflow axis, the compact central component exhibits a velocity gradient similar to the compact central component detected in CS(7–6).

We demonstrated that the model proposed by Takakuwa & Kamazaki (2011) cannot explain all of the observed properties of the CS(7–6) emission. Specifically, although their model predicts the presence of a compact central component, the observed velocity gradient of this component along the outflow axis is in the opposite direction to that predicted. Instead, all the observed properties of the CS(7–6) emission, along with the observed properties of the compact central component in ^{12}CO (2–1) and ^{13}CO(2–1), can be explained qualitatively if these emissions originate from inflowing gas along the outflow cavity walls carved into a rotating envelope. In this model:

1. The extended CS(7–6) component corresponds to the cavity walls closer to, and which therefore have larger projected extents on, the sky plane. Originating from infalling gas, the extended component therefore has a velocity gradient in the opposite direction to the bipolar CO outflow. If roughly in free fall, its velocity should increase inward from close to the systemic velocity at large radii, as is apparently observed. Because of stronger absorption in the deeper and cooler layers of the foreground envelope on its blueshifted side, this component is brighter on its redshifted side.

2. The compact central component originates from the cavity walls farther from, and which therefore have smaller projected extents on, the sky plane. Lying closer to the line of sight, this component therefore has a steeper velocity gradient than the extended component.
3. The velocity gradient across the outflow axis of both the compact and extended components is produced by the envelope rotation. The essentially constant velocity gradient exhibited by the extended component across the outflow axis away from the center indicates that the envelope rotates as a solid body out to a radius of $\sim 9''$ ($\sim$1800 au) along its equator.
4. The extended CS(7–6) component spans a range in radial velocities similar to that of the surrounding ambient cloud and hence is resolved out by the SMA in CO(2–1). By contrast, the compact central component spans a larger range in radial velocities that extends beyond that of the surrounding ambient cloud and can therefore be detected by the SMA not only in CS(7–6) but also in CO(2–1).

Finally, we investigate whether the proposed model can better explain the CS(7–6) emission of L1551-IRS5 and B335, both of which, like L483, have published ASTE+SMA maps. For L1551-IRS5, given present uncertainties in the geometry of the outflow cavities, we find that either our model or that proposed by Takakuwa & Kamazaki (2011) can provide viable explanations for its CS(7–6) emission. For B335, we show that the model proposed by Takakuwa & Kamazaki (2011) predicts the same direction in velocity gradient along the outflow axis for the CS(7–6) emission and bipolar CO outflow, whereas our model predicts opposite directions in velocity gradients as is observed.

The challenge of how bright CS(7–6) emission can be produced as far out as at least $\sim$4000 au from low-mass protostars remains even in our new model. We estimate that the emitting gas needs to have a density of $\sim 10^7\,\mathrm{cm}^{-3}$ if at a temperature of $\sim$10 K, or an order-of-magnitude lower density of $\sim 10^6\,\mathrm{cm}^{-3}$ if at a higher temperature of $\sim$40 K. By comparison, simple models for the envelopes of low-mass protostars indicate a density of only $\sim 10^5\,\mathrm{cm}^{-3}$ and a temperature of only $\sim$10 K at radial distances of a few thousand au from the center (e.g., Masunaga & Inutsuka 2000). Given a sufficiently luminous central protostar(s), it may be possible to heat the envelope surfaces defining the cavity walls to the required temperatures (e.g., Whitney et al. 2003). Although simulations by Machida et al. (2014) suggest that the cavity walls can be modestly enhanced in density by the bipolar outflow, the required enhancement in density may be more of a challenge.

Our study demonstrates that it is possible to trace infall and rotation in protostellar envelopes, at least along their outflow cavity walls, at radial distances within a few thousand au of the center. Observations with improved angular resolutions and sensitivities may better define the infall velocity as a function of radius. Furthermore, our study demonstrates that the detection of a relatively compact central component in protostellar envelopes through molecular lines tracing high densities and temperatures cannot be immediately assigned to a structure residing in the inner regions of the envelope such as a pseudodisk or perhaps even a circumstellar disk. Indeed, our model to explain the observed CS(7–6) emission of L483 requires no such structure.

J.L. acknowledges support from the Research Grants Council of Hong Kong through grant HKU 703512P.

REFERENCES

Arce, H. G., & Sargent, A. I. 2006, ApJ, 646, 1070
Beckwith, S. V. W., Sargent, A. I., Chini, R. S., & Guesten, R. 1990, AJ, 99, 924
Beltrán, M. T., Estalella, R., Anglada, G., Rodríguez, L. F., & Torrelles, J. M. 2001, AJ, 121, 1556
Chou, T.-L., Takakuwa, S., Yen, H.-W., Ohashi, N., & Ho, P. T. P. 2014, ApJ, 796, 70
Curtis, E. I., Richer, J. S., Swift, J. J., & Williams, J. P. 2010, MNRAS, 408, 1516
Ferreira, J. 1997, A&A, 319, 340
Frank, A., Ray, T. P., Cabrit, S., et al. 2014, Protostars and Planets VI, ed. H. Beuther et al. (Tucson, AZ: Univ, Arizona Press), 451
Fuller, G. A., Lada, E. A., Masson, C. R., & Myers, P. C. 1995, ApJ, 453, 754
Hartigan, P., Morse, J., Palunas, P., Bally, J., & Devine, D. 2000, AJ, 119, 1872
Hatchell, J., Fuller, G. A., & Richer, J. S. 2007, A&A, 472, 187
Hirano, N., Kameya, O., Nakayama, M., & Takakubo, K. 1988, ApJL, 327, L69
Jørgensen, J. K. 2004, A&A, 424, 589
Jørgensen, J. K., Bourke, T. L., Myers, P. C., et al. 2007, ApJ, 659, 479
Jørgensen, J. K., Schöier, F. L., & van Dishoeck, E. F. 2004, A&A, 416, 603
Leung, Y. C. 2015, Master's thesis, Univ. Hong Kong https://hub.hku.hk/handle/10722/221103
Lim, J., & Takakuwa, S. 2006, ApJ, 653, 425
Lim, J., Yeung, P. K. H., Hanawa, T., et al. 2016, arXiv:1607.00323
Machida, M. N., Inutsuka, S.-i., & Matsumoto, T. 2014, MNRAS, 438, 2278
Mardones, D., Myers, P. C., Tafalla, M., et al. 1997, ApJ, 489, 719
Masunaga, H., & Inutsuka, S.-i. 2000, ApJ, 531, 350
Momose, M., Ohashi, N., Kawabe, R., Nakano, T., & Hayashi, M. 1998, ApJ, 504, 314
Offner, S. S. R., Clark, P. C., Hennebelle, P., et al. 2014, Protostars and Planets VI, ed. H. Beuther et al. (Tucson, AZ: Univ, Arizona Press), 53
Offner, S. S. R., Lee, E. J., Goodman, A. A., & Arce, H. 2011, ApJ, 743, 91
Pudritz, R. E., Ouyed, R., Fendt, C., & Brandenburg, A. 2007, Protostars and Planets V, ed. H. Beuther et al. (Tucson, AZ: Univ, Arizona Press), 277
Pyo, T.-S., Hayashi, M., Kobayashi, N., et al. 2002, ApJ, 570, 724
Sault, R. J., Teuben, P. J., & Wright, M. C. H. 1995, in ASP Conf. Ser. 77, Astronomical Data Analysis Software and Systems IV, ed. R. A. Shaw, H. E. Payne, & J. J. E. Hayes (San Francisco, CA: ASP), 433
Seale, J. P., & Looney, L. W. 2008, ApJ, 675, 427
Shirley, Y. L., Evans, N. J., II, Rawlings, J. M. C., & Gregersen, E. M. 2000, ApJS, 131, 249
Shu, F. H., Shang, H., Glassgold, A. E., & Lee, T. 1997, Sci, 277, 1475
Tafalla, M., Myers, P. C., Mardones, D., & Bachiller, R. 2000, A&A, 359, 967
Takakuwa, S., & Kamazaki, T. 2011, PASJ, 63, 921
Takakuwa, S., Kamazaki, T., Saito, M., Yamaguchi, N., & Kohno, K. 2007, PASJ, 59, 1
van der Tak, F. F. S., Black, J. H., Schöier, F. L., Jansen, D. J., & van Dishoeck, E. F. 2007, A&A, 468, 627
van Kempen, T. A., Kristensen, L. E., Herczeg, G. J., et al. 2010, A&A, 518, L121
Velusamy, T., Langer, W. D., & Thompson, T. 2014, ApJ, 783, 6
Visser, R., Kristensen, L. E., Bruderer, S., et al. 2012, A&A, 537, A55
Whitney, B. A., Wood, K., Bjorkman, J. E., & Cohen, M. 2003, ApJ, 598, 1079
Wu, P.-F., Takakuwa, S., & Lim, J. 2009, ApJ, 698, 184
Yen, H.-W., Takakuwa, S., & Ohashi, N. 2010, ApJ, 710, 1786
Yen, H.-W., Takakuwa, S., & Ohashi, N. 2011, ApJ, 742, 57